Research Square

Preprints are preliminary reports that have not undergone peer review.
They should not be considered conclusive, used to inform clinical practice,
or referenced by the media as validated information.

A New Insight into Cutting and Chip Formation Mechanisms in Ultrasonic Vibration-Assisted Drilling via Kinematic Modeling, Experiments, and Finite Element Analysis

Muhammad Fadhlan Afif

mfafif0002@gmail.com

King Fahd University of Petroleum & Minerals https://orcid.org/0009-0001-9807-546X

Jiunn-Jyh Wang

Ahmed Aly Diaa Sarhan

Research Article

Keywords: machining, finite element analysis, kinematics, ultrasonic vibration-assisted drilling, chip formation

Posted Date: June 29th, 2026

DOI: https://doi.org/10.21203/rs.3.rs-9974453/v1

License: This work is licensed under a Creative Commons Attribution 4.0 International License.
Read Full License

A New Insight into Cutting and Chip Formation Mechanisms in Ultrasonic Vibration-Assisted Drilling via Kinematic Modeling, Experiments, and Finite Element Analysis

Muhammad Fadhlan Afif[1], Jiunn-Jyh Wang[2], Ahmed Aly Diaa Sarhan[1,3*]*

[1] Department of Mechanical Engineering, King Fahd University of Petroleum & Minerals, Dhahran 31261, Saudi Arabia, g202304230@kfupm.edu.sa

[2] Department of Mechanical Engineering, National Cheng Kung University, Taiwan, jjwang@mail.ncku.edu.tw

[3] Interdisciplinary Research Centre for Intelligent Manufacturing & Robotics, King Fahd University of Petroleum and Minerals, Dhahran 31261, Saudi Arabia, ahsarhan@kfupm.edu.sa

*Corresponding author

**Ahmed A.D. Sarhan*, ahsarhan@kfupm.edu.sa

**Muhammad Fadhlan Afif*, g202304230@kfupm.edu.sa

Abstract

Ultrasonic vibration-assisted drilling (UVAD) significantly enhances machining performance by reducing cutting forces, extending tool life, and improving chip evacuation. While parameter optimization is well-documented, a fundamental gap remains in understanding how processing parameters drive underlying mechanisms at the elemental scale. This study addresses this gap by establishing a novel kinematic framework of the elemental cutting edge to model alternating cutting velocities, penetration angles, and tool-chip contact interfaces, subsequently deriving the machined surface topology and varying effective uncut chip thickness caused by micro-hammering mechanism. Furthermore, an explicit dynamics finite element analysis (FEA) utilizing Arbitrary Lagrangian-Eulerian (ALE) adaptive meshing reveals that performance gains stem from alternating effective rake angles, reduced contact lengths, increased chip curvature, and compressive residual stresses, yielding sawtooth-like chip profiles and a four-fold improvement in chip breakage. Crucially, the study results challenge the widely accepted interrupted cutting mechanism in UVAD. It is demonstrated that at ultra-low feeds, complete tool-workpiece separation is inhibited by a physical loading effect that dampens vibration amplitudes, alongside the inherent stickiness of ductile materials, proving that the improvements resulted within continuous tool-chip interface modulation rather than macro-separation. Under applicable feeds, these mechanisms are experimentally validated through reduced cutting forces and comprehensive chip topology analysis. The presence of unique oscillation traces, thinner chips, and a lower chip compression ratio confirms a marked reduction in chip evacuation forces. Ultimately, these insights provide a new paradigm for validating and optimizing vibration-assisted machining systems.

Keywords: machining, finite element analysis, kinematics, ultrasonic vibration-assisted drilling, chip formation

1. Introduction

In manufacturing industries, including aerospace, automotive, and precision machinery, more advanced and higher performance materials are used. Some of these materials are categorized as hard-to-cut materials which is combined with additional considerations, such as thin-wall, tight-tolerance, chatters prevention, dry cut, zero defect, high reliability, or challenging machining feature, becomes even hard to anticipate [1–12]. Ultrasonic vibration-assisted machining (UVAM) has been shown to become the solution to machine the hard-to-cut materials [13–18]. The process involves superimposing low amplitude (around 1-20 μm) and high frequency (more than 20 kHz) vibration in different directions depending on the machining processes [19–23]. The qualities of the drilling process in UVAM are improved in terms of cutting forces, surface quality, tool life, defect reduction and dimensional accuracy [24–30].

The applications of ultrasonic vibration assistance in machining have been reported to be applied to different machining types and vibration conditions to cut several materials [31–34]. Zhang et al. [35] developed a UVAM in 2D direction for milling operation of CF/PEEK composites. The direction of vibration assistance is on the feed and vertical direction of the tool. The optimum cutting parameters are obtained through experiments related to theoretical studies. Namlu et al. [36] investigates the multi-axial UVAM and nanofluid lubrication for machining Ti-6Al-4V in slot milling operation with minimum quantity lubrication (MQL). The experiments show the reduced cutting forces up to 37.6% and surface roughness up to 37.4%. The study also inferred that the surface textures promote machining efficiency and precisions for machining this material. Blasl et al. [37] did some experimentation for the same method and materials except they used cryogenic MQL. Reduced tool wear and improve tool life are found even though they found higher surface roughness on the surface. On the other hand, Chaudhari et al. [38] reports that the UVAM has been shown to improved surface integrity machine hardened materials while demonstrating reduced plastic strain and lower thermo-mechanical loads. Moreover, Hap et al. [39] explain the tool wear reduction in UVAM for PCD cutter upon cutting SiCp/Al composite. The study determines the cutting parameters which are optimized for combination of the tool and the workpiece. Liu et al. [44] shows that there are different defects on machining carbon fiber-reinforce carbon matrix (C/C) and UVAM to be solution to reduce the defects. The stress peaks and a combined compressive-shear stresses results in micro fractures and reduction of fiber deformation which ultimately improves the machining process.This indicates that there are different preferable cutting conditions which highly depends on the techniques or materials being used thus optimization is required.

Notably, experimental studies have been done to determine the optimum cutting parameters upon deploying UVAM through kinematical approaches. Ni and Zhu [40] studied the UVAM for milling process on TC4 alloy with MQL technology. Different cutting parameters are explored to determine the best obtainable machine surface roughness, profile, and chip morphology. The study also includes tool-tip trajectories as one of basis to justify the experimental findings. Zhao et al. [41] performed optimization on cutting parameters for minimum

machining deformation with UVAM on thin-walled workpieces. The multi-objective optimization is done to determine the optimum cutting parameters while the ultrasonic amplitude ratio is fixed as 80%. Xu et al. [42] investigates the machinability of micro holes for ceramic matrix composites through ultrasonic drilling with grain-based cutting tools. Different cutting parameters are observed corresponding to their performance in terms of tool wear/fracture, burs, and cutting forces. This study also includes cutting trajectory models where the tool tip intermittent contact is found and acts as foundation to develop the cutting force models. Gao et al. [43] apply the vibration assistance in milling for internal threads in superalloy workpiece material, specifically focuses on the wear mechanisms and machining performance. The study shows that the adhesion and abrasive wear of the tool are highly reduced along with higher thread quality.

It is important to notice that the optimizations of the cutting parameters for different applications have been studied in literature. However, the understanding of the mechanism within the process is becoming more important and requires further studies. Understanding the process mechanism is essential in maximizing its productivity and application to process other hard-to-cut materials. The standardization and best practices for material-specific guidelines require further understanding of the mechanism and further improved in future research.

Several efforts have been made by researchers to understand the process mechanisms and build the process models. Ni et al. [45] modeled contact rate between tool and workpiece for UVAM on milling of Ti-6Al-4V. They inferred that the contact-separation causes complexity of intermittent machining in UVAM. Verma et al. [46] proposed a cutting force model for UVAM in milling process that includes acoustic softening-intermittent cutting, and end mill helix angle. Xie et al. [47] develop a cutting model specifically for fiber reinforced matrix that considers the deformation and fracture modeling also debonding. While it is still limited to 90^{o} fiber orientation, it also only focuses on the fiber debonding. Chen et al. [48] study the transient thermo-mechanical coupling mechanism that mainly focuses on the chip formation process for UVAM in turning with dry conditions. In addition, the model also incorporates the shear zone modelling thus able to predict the cutting forces with adequate accuracy and tool-chip interface effect. Yin et al. [49] developed a UVAM system that applies the vibration in tangential direction for turning titanium alloy slender shaft. The process model explores the chip geometries of different cutting modes and Johson-Cook constitutive model as main fundamental of the cutting process and Euler-Bernoulli beam theory to accommodate the dynamics aspects of the turning process. Study by Yin et al. [50] proposed the sophisticated model of the UVAM that details the chip load and considering the phase lag effect on the cutting process. The study also found that the process temperature in UVAM is reduced especially for hard-to-cut materials turning process.

In addition, Song et al. [51] showed that the ultrasonic assistance promoted plastic removal due to pulling effect and enhanced instantaneous forces in the scratching of Fe-Cr alloys. Reflecting this study, further investigation required if the same insight applies on the UVAM in macroscale. Teng et al. [52] study an interesting finding

where the dicing mechanism that promotes brittle-ductile characteristic is revealed during the ultrasonic vibration-assisted blade dicing. They claimed that the periodic contact and separation between tool and workpiece affect the material removal mechanism. Sun et al. [53] concluded that Poisson's ration affects the machining accuracy and tool wear improvement in the ultra-precision turning. It is revealed that the oscillation trajectory becomes arc rather than a straight line even though the vibration assistance direction is in one dimension. This infers that further kinematical study should be done to clearly characterize the UVAM. Zhang et al. [54] develop an ultrasonic-assisted milling model for cutting predictions along with the tool wear model specifically for the application on Ti-6Al-4V. The study discusses the uncut chip thickness for the force prediction. It is clearly stated that separation and contact are depicted to be one of the mechanisms in the ball-end milling process.

Several studies use finite element analysis (FEA) to understand the cutting process [55] and ultrasonic vibration effects that occur in high-speed and micro scale such that they cannot easily be observed in real cutting process [56,57]. One of notable study is done by Cui et al. [58] where they developed a multiscale simulation on UVAM for composite materials that consider the acoustic softening effect. The analysis mainly focusses on the orthogonal cutting setup on the SiCp granules that are embedded on the Al matrix. The stress reduction of the matrix, microscopic removal mechanism, stress relaxation, and finely broken SiC particles are demonstrated in the analysis and claimed as factors that promote performance improvement. Hu et al. [59] developed a 3D FEA for longitudinal bending hybrid UVAM based on the proposed cutting trajectory where the chip formation and surface roughness can be observed to support the reasoning of the experimental findings. Kim et al. [60] developed FEA model to observe the effect of laser assistance and ultrasonic vibration assistance in turning process. The effect of the laser parameters and cutting parameters can be directly observed in the FEA. Gao et al. [61] observed ultrasonic drilling where the axial and torque are predicted through probability density function of the height distribution. The study also employed single grain FEA upon contacting the 3C-SiC through the abrasive process. The scratching forces under different parameters become foundation to develop the proposed prediction model with 11.14% and 27.43% errors of axial force and torque. This indicates that the FEA analysis could be useful to study UVAM even though connecting its results to other modelling techniques requires excellent framework and techniques.

Undoubtedly, conventional drilling (CD) models are the foundation for developing a more advanced drilling process. It started with utilization of the cutting theory to simulate the torque and thrust forces that highly depend on the cutting tool geometry and workpiece materials [62]. The twist drill bit can be defined through oblique cutting framework where the inclination, rake, and clearance angle vary radially, while the distinct chisel edge geometry near the center of drill is quite constant radially [63–66]. Chip evacuation resistance is introduced from friction between the chip and surroundings during evacuation explains the increased cutting forces and chip thickness as drilling depth progress [67,68].

In low-frequency vibration-assisted (LVAD), higher amplitudes with low frequency of vibration assistance are utilized and the cutting force model has been developed based on the orthogonal cutting theory and validated with experiments [69,70]. The main cutting mechanism fundamentally depends on the interrupted cutting trajectory that causes chip discretization [71]. Authors argue that the insights from LVAD studies somehow have been extended to ultrasonic vibration assisted drilling (UVAD) in literature without providing comprehensive studies and evidence.

While some of the studies on UVAM have previously mentioned, this is also noted that few research that discussed the process mechanism specifically in UVAD. Neugebauer [19] shows that the ultrasonic vibration influences the chip breakage. He also claimed that there are alterations in cutting velocity and angles. Chen et al. [72] derived the kinematics model of UVAD by regarding the tool as a cutting point. It showed that even in the interrupted cutting trajectories, the chips are not discretized as expected. Chen et al. [73] also showed chip shapes from processes with different cutting parameters in UVAD. The better surface topology and chip breakage are obtained even though it is not directly related to the presented kinematics analysis as also observed in study by Duman et al. [74]. Georgi et al. [75] study focused on acoustics measurement. They observed the frequency changes with and without cutting while discussing the phase lag change in UVAD. In addition, Zhang, et al. [76] developed a model in ultrasonic-assisted friction drilling on Ti-6Al-4V that mainly involved thermal softening effect under seven distinct phases upon drilling progression resulting in chipless result. Despite the reasonable accuracy, the application of the model to other material types needs to be investigated further. Zhang et al. [77] showed that there are different modes of cutting process depending on the orientation of the fiber in the ceramic matrix composite. The nature of the materials that involve brittle materials determines the different mechanisms compared with cutting process in ductile materials [78].

Öztürk [79] performed FEA for UVAD using a micro-textured drill bit to demonstrate the effectiveness of the drill bit to reduce cutting forces. This study is assumed to be close to the current study, except that his study simulates the whole drill bit. In addition, Xu et al. [80] also did similar FEA for UVAD that includes the whole drill bit in the simulation for stacked workpieces. Even though drilling performance such as chip evacuation in the groove, lower thermal and cutting forces can be observed, the reasons behind these still need to be investigated. Authors argue that the current study could provide more insights through different approaches to the understanding of UVAD in literature. The study on UVAD still lacks due to the high-speed phenomena and the complex cutting process in nature at very limited access to directly observe the process. The optimized cutting parameters are highly dependent on the cutting conditions (such as tool geometries, tool materials, or workpiece materials, etc.) without the common ground that is explainable for almost all cases.

This paper aims to unveil the process mechanisms and chip formation in UVAD through kinematics that also address the importance of tool edge geometry of the drilling tool. The interaction between the tool motion upon contact with the workpiece is observed to arrive at the uncut chip thickness variation that depends on the

machined surface profile. The FEA is performed to study the high-speed phenomena that occur during the drilling process. Moreover, the effect of vibration assistance on chip formation, thrust force and cutting torque are discussed based on the analysis and findings. In Section 2, the kinematics of UVAD is derived while considering the tool edge geometry of the cutting points along the cutting edge. The cutting trajectory, uncut chip thickness, cutting velocities and penetration angles are found to be varying along the radius and drilling progression. In Section 3, the machined surface profile is determined through the analysis of the tool edge with its geometry that moves along the cutting trajectory and penetrates the cut surface causing the micro hammering effect. The machined surface profile function is derived to determine the real uncut chip thickness variation between successive cuts. In Section 4, the finite element analysis is discussed whereas several cutting mechanisms that support the drilling performance improvement are unveiled. It is followed by experimental verification in Section 5 where the chip topology, morphology and cutting forces are discussed that indicates the better drilling performance as found in the FEA.

2. Kinematics of ultrasonic vibration-assisted drilling

This section focuses on defining the moving cutting-edge geometry along the cutting trajectories. Notably that the elemental cutting edge is considered in which the geometry and cutting speeds vary along the radius of drill bit. Therefore, the uncut chip thickness can be defined along the drilling progressions for any cutting parameters or tool geometry. Moreover, the cutting velocities and angles are shown to vary along the drilling progression and radius in this section.

2.1 Elemental cutting edge geometry

The cutting-edge geometry is defined by using the common and easy-to-measure dimensions to come up with the elemental cutting-edge geometry. The elemental cutting edge which can be referred as cutting point is indefinitely small and varying along the cutting-edge radius. The cutting process is expected to occur on all cutting points with specific geometry cumulatively results in chip formation and cutting forces [63,81,82].

The geometric features of a twist drill are shown in Figure 1. These are pointing angle (ρ), outer helix angle (δ_R), chisel edge angle (θ_e), and half of the web thickness (W). The cutting edge consists of two parts which are the chisel edge and cutting lip. The geometrical features are used to determine the tool edge geometry on the chisel edge and cutting lips that consist of rake angle (α) and clearance angle (γ) where they are the functions of cutting point radius r. Two opposite cutting edges at the same radius cut the material at the same time. Cutting point in cutting edge 1 is addressed as cutting point 1 denoted as p_1, and respectively for cutting point 2 denoted as p_2. In this paper, the cutting edges are divided into elements located on cutting points. The cutting points are observed while following the rotation and oscillation motion.

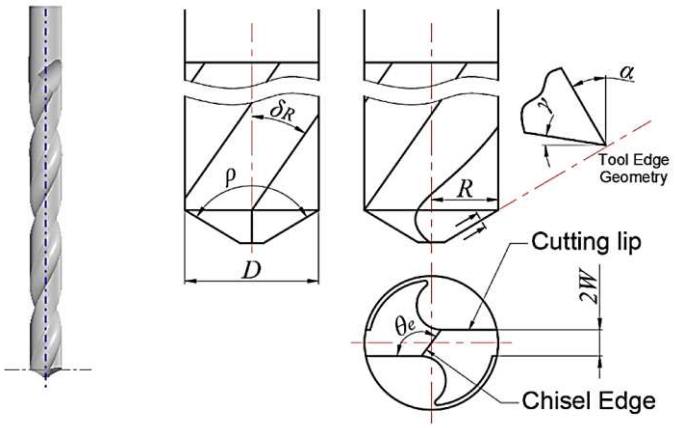


Figure 1. Geometrical features of twist drills that are used to determine the cutting point geometry at chisel edge and cutting lip

The cutting process on chisel edge consists of indentation and extrusion processes. The indentation zone is where the cutting point r is less than the radius of the indentation zone (R_i). It is regarded as a wedge indent and extrudes the material in this zone [83–85]. Therefore, R_i can be expressed as follows

$$R_i = \frac{t_{z0}\, n_f}{2\tan\left(\frac{\pi}{2} - \rho\right)}, \tag{1}$$

where ρ is the drill point angle as shown in Figure 2. Moreover, t_{z0} is the feed per tooth and n_f is the number of flutes.

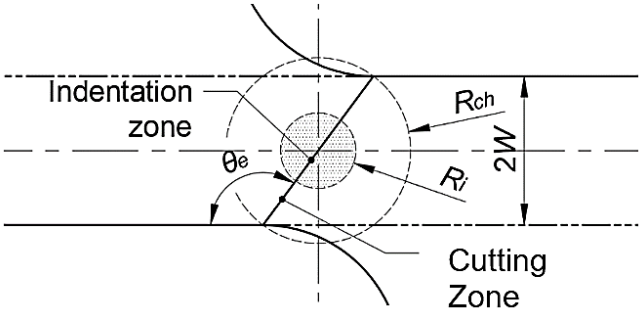


Figure 2. Dimensions and division of chisel edge region into indentation and cutting zone

In the cutting zone, the cutting process can be regarded as an orthogonal cutting with a negative rake angle and a very slow V_t. This cutting process occurs when the r is between R_i and chisel edge radius (R_{ch}) [83–85]. The R_{ch} can be expressed as:

$$R_{ch} = \frac{W}{\sin(\pi - \theta_e)}, \tag{2}$$

where W is half the thickness of the drill web and θ_e is the chisel edge angle. According to Chandrasekharan et al. [86], the rake angle of the chisel edge (α_{ch}) is:

$$\alpha_{ch} = -\tan^{-1}(\tan p \cos(\pi - \theta_e)). \tag{3}$$

The cutting lip has a longer portion in the cutting edge compared with the chisel edge region. Therefore, most of the cutting process occurred in this region. The derivation of variables in the cutting lip considers the orthogonal cutting theory of Ernst and Merchant [87], Stabler [88] and the relational expressions of various angles refer to Armarego and Cheng [63]. Then, the inclination angle of the drill (i), web angle (ω), and the helix angle (δ) along the radius can be determined by the following equations:

$$\begin{aligned} \sin i &= \sin\omega \sin p \\ \omega &= \sin^{-1}(W/r) \ , \\ \delta &= \tan^{-1}(2\pi r/L_p) \end{aligned} \tag{4}$$

Armarego and Cheng [63] proposed an equation to determine the equivalent rake angle (α_q) in orthogonal cutting that approximate the normal rake angle (α_n) which is inclined in oblique cutting for any corresponding cutting point. These rake angles can be evaluated through

$$\begin{aligned} \tan\alpha_n &= \frac{\tan\delta}{\sin\rho}(\cos\omega + \sin\omega\tan\omega\cos^2\rho) - \tan\omega\cos\rho \\ sin\alpha_e &= sin^2 i + cos^2 i\ sin\alpha_n. \end{aligned} \tag{5}$$

Moreover, both variables are functions of i and ω, so that the α is varying with the radius on the cutting lip as shown in Figure 3. For the twist drill geometry used in this study, which is shown in Table 1, the analytical values are plotted as continuous line while the measured values are plotted as red scatter point at certain value of r by using the white light interferometry. The clearance angle γ may vary along the radius or constant depending on the tool specifications. While the drill bit is divided into chisel edge and cutting lip region, this study focuses on the cutting lip region where the main cutting process occurs.

Table 1. Drilling tool specification



Model	NACHI SGESS LIST7572P
Diameter (D) [mm]	6
Material	Powdered HSS (TiCN Coating)
Number of blades (n_f)	2
Tool nose radius (r_ε) [mm]	0.014
Length (L) [mm]	70
Tool Overhang (L_{OH}) [mm]	45
Drill Point Angle (ρ) [deg]	135
Outer Helix angle (δ_R) [deg]	30
Drill Margin ($2W$) [mm]	0.95
Chisel edge angle (θ_ε) [deg]	157
Tool Flute length (L_f) [mm]	25
Clearance Angle (γ) [deg]	9 (constant)

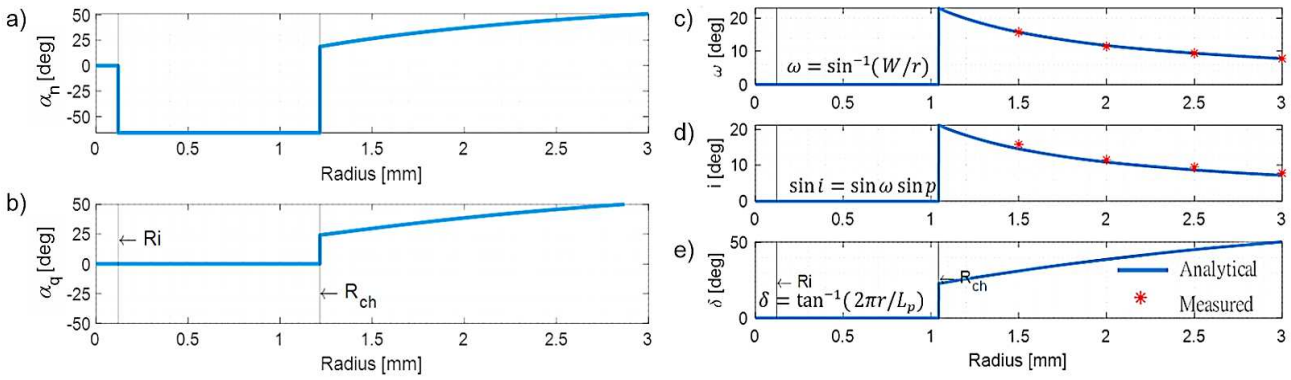


Figure 3. The cutting point geometry along the radius of drill bit: (a) normal rake angle, (b) equivalent rake angle, (c) web angle, (d) inclination angle, (e) helix angle

2.2 *Elemental cutting edge trajectories*

The cutting points are now regarded as moving along the trajectories. The trajectories are highly dependent on the cutting parameters and vary along the radius. The derivations are discussed with enough detail to represent the complex drill bit geometry that has been used for granted in the drilling process.

As shown in Figure 4, a cylindrical coordinate system r, θ, z is used to represent the cutting point position. The local coordinate origin is located at the initial position of the imaginary bottom tip of cone of the drill. A more detail on the dimensions and parameters involved are shown in Figure A.1 in Appendix. The center of the drilling tool coincides with the z-axis of the local coordinate. The cutting points are following the motion which depends on parameters. The drilling parameters consist of s and feed per tooth (t_{z0}), while the oscillation parameters consist of oscillation frequency (f_0) and amplitude (A_0). The position of the cutting points can be expressed as:

$$\begin{aligned} p_1(r) &= (r, \theta, p_z + p_{z_o}) \\ p_2(r) &= (r, \theta + \pi, p_z + p_{z_o}), \end{aligned} \tag{6}$$

where θ is the angular position of the cutting point that consider the web angle (ω) and angular displacement (φ) so that:

$$\begin{aligned} \theta &= \varphi + \omega \\ \varphi &= 2\pi s t \\ \omega &= tan^{-1}\left(\frac{W}{r}\right) \end{aligned}, \tag{7}$$

while s is the rotation per second.

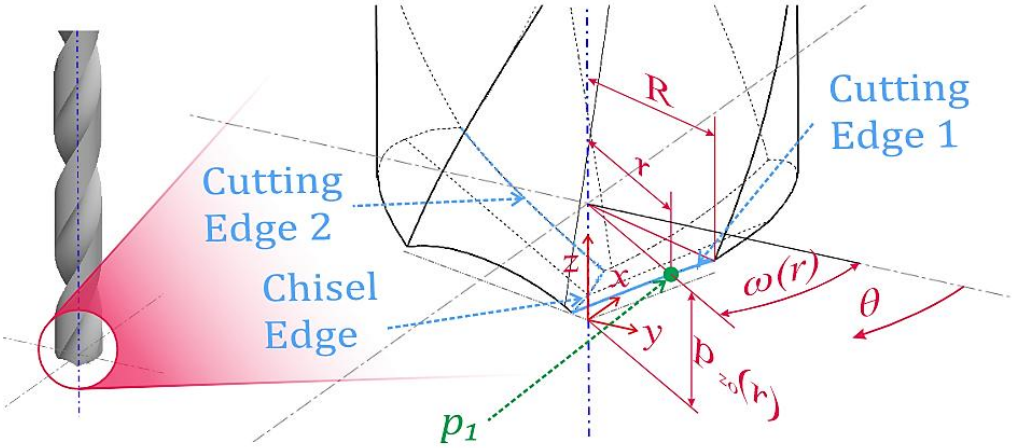


Figure 4. Cutting point position p_1 on a twist drill with respect to the coordinate system, which illustrates the initial position of the cutting point and how it moves on drilling progression

Note that p_z and p_{zo} are the absolute position and the initial position of the cutting point in the z-direction, respectively. The p_{zo} is addressed due to the presence of a drill point angle (ρ). In Figure 4, the value of p_z is initially zero, meanwhile, the p_{zo} can be expressed as

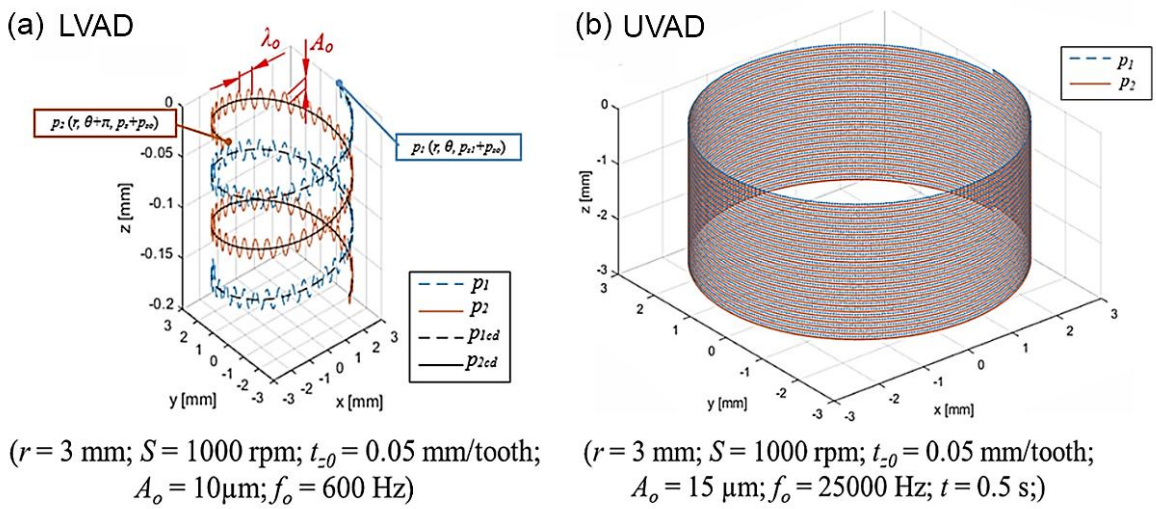
$$p_{z_o} = r\,tan^{-1}\left(\frac{\rho}{2}\right). \tag{8}$$

Figure 5 depicts the cutting point positions during a certain interval of time (t). In UVAD, the motion in CD is superimposed with the oscillation motion that comes from the vibration assistance in the feeding direction. For illustration purposes in Figure 5 (a), f_o is set as very low as in LVAD only to clearly show the motion within the derived kinematics model. Note that p_{1cd} and p_{2cd} are the position of cutting point for CD only. In Figure 5(b) the real f_o used in UVAD is shown such that the scale proportion between the A_o and R can be seen. The positions of cutting point 1 and cutting point 2 in the z-direction ($p_{z1,2}$) can be expressed as:

$$p_{z_{1,2}} = -f_z st + A_o\,sin(2\pi f_o t) \tag{9}$$

$$f_z = t_{zo} n_f,$$

where f_z is the feed per revolution. Note that n_f is the number of flutes which is in this case is two.



($r = 3$ mm; $S = 1000$ rpm; $t_{z0} = 0.05$ mm/tooth; $A_o = 10\mu$m; $f_o = 600$ Hz)

($r = 3$ mm; $S = 1000$ rpm; $t_{z0} = 0.05$ mm/tooth; $A_o = 15$ µm; $f_o = 25000$ Hz; $t = 0.5$ s;)

Figure 5. Cutting point trajectories of two cutting points in vibration-assisted drilling. (a) low frequency vibration-assisted drilling (LVAD). (b) ultrasonic vibration-assisted drilling (UVAD)

2.3 *Uncut chip thickness*

The cutting point trajectories are used to define the uncut chip thickness which determines the load during drilling process. Uncut chip thickness (t_z) is defined by the distance between two successive trajectories as shown in Figure 5. Thus, the position of cutting points in the previous half trajectory should be determined.

At the same time, the uncut chip thickness of cutting edge 1 (t_{z1}) and cutting edge 2 (t_{z2}) are different because they are in the opposite directions and depends on the successive cut. Both can be evaluated by:

$$\begin{aligned} t_{z1} &= p_{z_1}(t) - p_{z_2}(t-T) \\ t_{z2} &= p_{z_2}(t) - p_{z_1}(t-T), \end{aligned} \tag{10}$$

where T is the time delay between two successive cuts calculated as half of period of rotation $(1/2s)$.

The cutting point trajectory can be shown in a 2D plane by considering the helical travel distance (h) as shown in Figure 6. The p_{z1} and p_{z2} are plotted against h, so t_z variation and the wavelength (λ_o) can be determined as previously shown in Figure 5. Those values are determined by using the following equation

$$\begin{aligned} h &= st\sqrt{f_z{}^2 + (2\pi r)^2} \approx 2\pi srt \\ \lambda_o &= h(t+t_o) - h(t), \end{aligned} \tag{11}$$

where t_o is the period of oscillation.

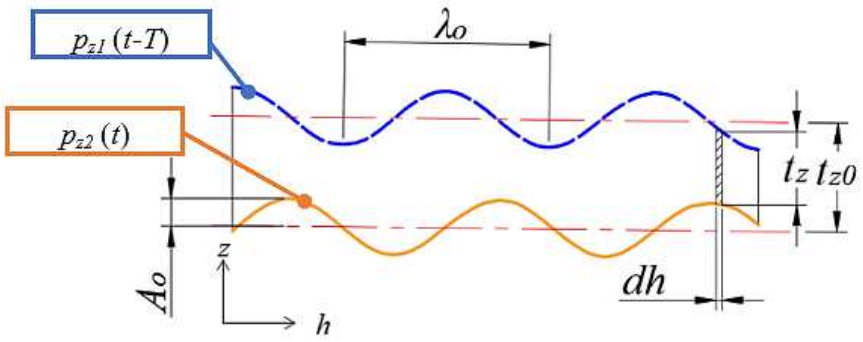


Figure 6. Cutting point trajectory in a 2D plane

2.4 Cutting velocities and penetration angle

The cutting trajectory also infers the process parameters which are important in the drilling process. The cutting velocities and the penetration angle in UVAD are shown to be different compared with CD. The penetration angle is derived to determine when the flank face of the tool is in-contact with workpiece.

The cutting velocity can be expressed in the tangential and axial direction and be shown in a 2D cutting point trajectory as shown in Figure 7. Thus, the tangential velocity (V_t) is constant and can be expressed as:

$$V_t = \theta' r = 2\pi sr. \tag{12}$$

Meanwhile, axial velocity (v_z) and its maximum value (Vz) can be expressed as:

$$v_z = z' = 2A_o\pi f_o \cos(2\pi f_o t) \tag{13}$$

$$V_z = 2A_o\pi f_o \ .$$

Moreover, the resultant cutting velocity (v_c) and the corresponding maximum value (V_c) be expressed as:

$$\begin{aligned} v_c &= \sqrt{{V_t}^2 + {v_z}^2} \\ V_c &= \sqrt{{V_t}^2 + {V_z}^2}. \end{aligned} \tag{14}$$

The penetration angle (κ) is defined as the angle between v_c and v_t. It shows the direction of the cutting point movement along the oscillation trajectory. Moreover, the maximum value of κ is denoted as K. These can be expressed as:

$$\kappa = tan^{-1}\left(\frac{v_z}{V_t}\right) \tag{15}$$

$$K = tan^{-1}\left(\frac{V_z}{V_t}\right).$$

It is noticeable that the flank face hit the currently generated surface profile upon the κ value is positive which indicates that the cutting point is currently going down at the time.

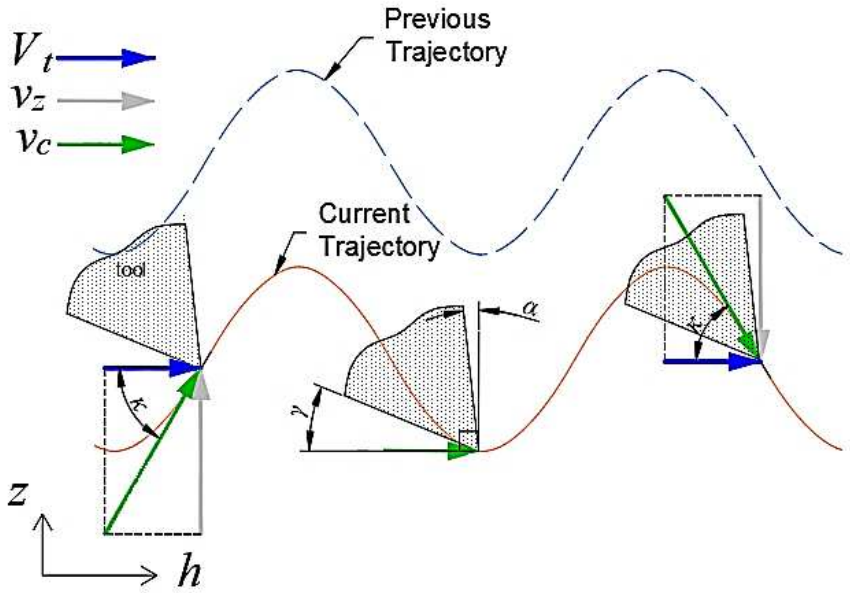


Figure 7. Cutting velocities and penetration angle variation along with the oscillation motion

3. Machined surface profile topology

The resulting machined surface profile topology are discussed in this section. The mathematical models are derived based on the kinematical studies discussed in the previous section. The penetration angle κ indicate the micro hammering effect that creates distinct machined surface profile topology. Therefore, the effective uncut chip thickness depends on the topology and is shown to be specifically for UVAD and different from some studies in literature.

3.1 Machined surface profile derivation via micro hammering effect

In UVAM, distinct texture can be observed or even engineered to gain specific tribological function [89,90]. This involves micro hammering mechanism that influences the machined surface profile. Some references addressed this phenomenon [42,69,75,91], even though the topology is not yet discussed in detail specifically for drilling process. The micro hammering mechanism is the formation of the machined surface profile caused by the flank face with a value of γ that compresses and extrudes a certain volume of material to the free space as the tool penetrates the workpiece.

Figure 8 describes the cutting point geometry motion for two cycles of oscillation in steps. Because of the micro hammering effect, the machined profile is not sinusoidal, instead it has a periodic sawtooth-like profile.

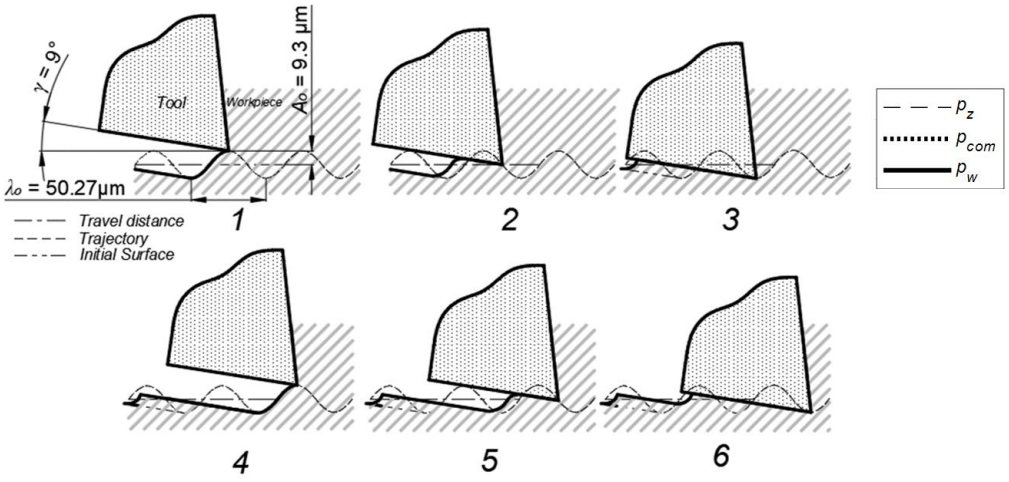


Figure 8. Illustration of micro hammering mechanism resulted in saw-tooth-like profile (r = 3 mm; γ = 9°; S = 4000 rpm; f_o = 25000 Hz; A_o = 9.3 µm)

The workpiece machined surface profile (p_w) can be characterized by several geometric measures as shown in Figure 9. The λ_o of p_w is the same as in p_z. Moreover, there are slope length (L_w) and height (H_w) of the machined profile. There is also an intermediate profile that represents the initial cut surface and the compressed profile without the extrusion process (p_{com}). The shape of p_w is constrained by the p_{com} and tool flank. Thus, it is assumed that p_w has the same shape as p_{com}. Further details on the geometrical analysis to come up with the following equations are shown in Figure A.2 on the Appendix.

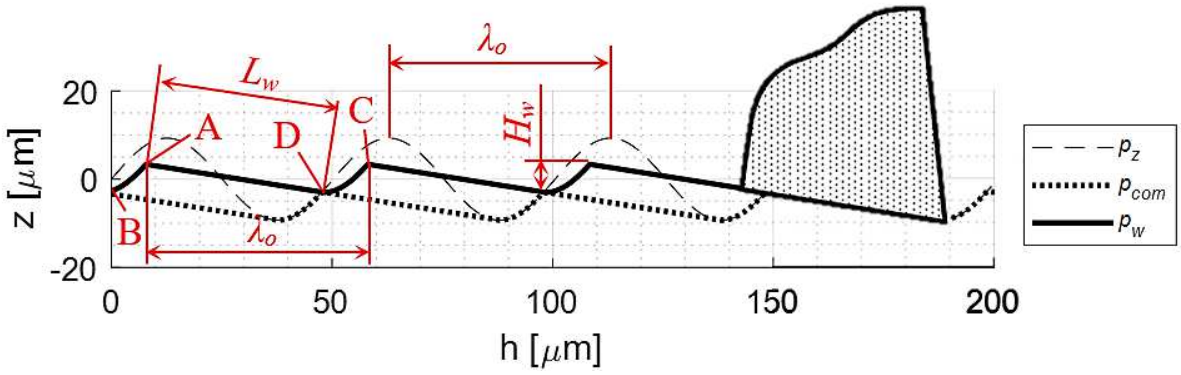


Figure 9. The machined surface profiles due to micro hammering effect

The η is the angle that represents the ratio of oscillation magnitude and wavelength as shown in Figure A.2 on the Appendix. It can be evaluated as:

$$\eta = tan^{-1}\left(\frac{4A_o}{\lambda_o}\right). \tag{16}$$

After that, the slope length of L_w, which is equal to p_{com} (L_{com}), and the height of profile H_w, that is equal to can be p_{com} (H_{com}) are evaluated as:

$$L_w = \frac{\lambda_o \sin\eta}{\sin(180^\circ - \gamma - \eta)} \tag{17}$$

$$H_w = L_w \sin\gamma.$$

The extruded area can be determined through the width (W_{ext}) and length (L_{ext}) of the extruded area which can be expressed as:

$$L_{ext} = \frac{U_{ext}}{W_{ext}} \tag{18}$$

$$W_{\text{ext}} = \lambda_o \sin\gamma.$$

Under the different values of A_o, λ_o and r, the value of H_w can be evaluated and shown in Figure 10. It is shown that the higher A_o and λ_o give the higher H_w. Moreover, it can be inferred that the H_w varies with the radius of the cutting point in drilling as the λ_o varies with radius even under the same cutting parameters.

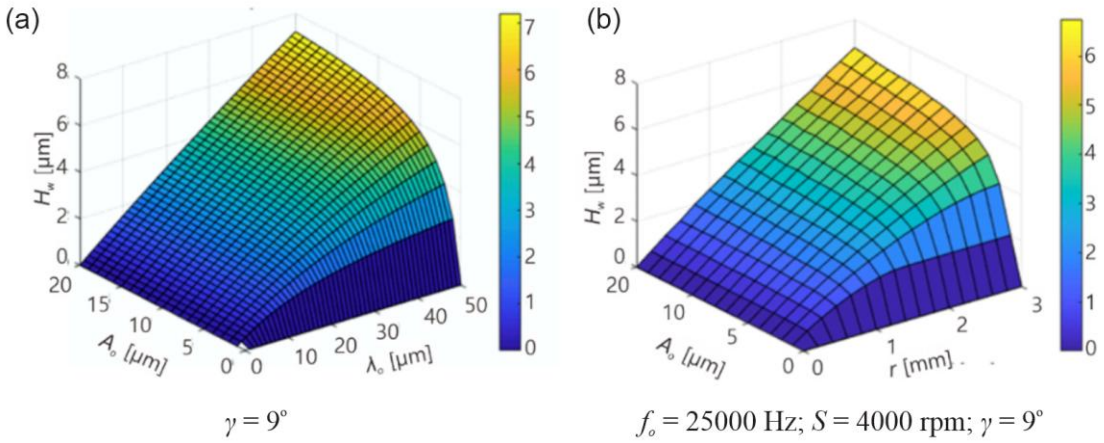


Figure 10. Variation of wiped profile height under different oscillation parameters. (a) varies with wavelength. (b) varies with radius

3.2 Effective uncut chip thickness

The effective uncut chip thickness is now defined as the distances between the current cutting trajectory against the successive machined surface profile. It is shown to vary along with the drilling progression.

The same procedure, as shown in Section 2.3, is taken to evaluate the effective uncut chip thickness (t_{ze}). For a certain value of r, one can evaluate the t_{ze} as shown in Figure 12 as follows:

$$t_{ze} = p_w(t - T) - p_z. \tag{19}$$

In Figure 11, the t_{ze} variation of certain drilling and oscillation parameters is shown. During the cutting process, the previous cut surface follows p_w. Meanwhile, the current tool motion is moving along with the oscillation trajectory that considers the effective oscillation amplitude (A_{oe}) and effective oscillation frequency (f_{oe}) affected

by the loading effect. One can use the same kinematics and machined surface profile model to determine the effective oscillation trajectory, generated surface profile and uncut chip thickness along with the drilling progression with a given A_{oe} and f_{oe}. Note that at different phase angles, the t_{ze} has different variations overtime or drilling progression. This t_{ze} variation is an interesting point to be noted as it might influence the improvement of drilling performance.

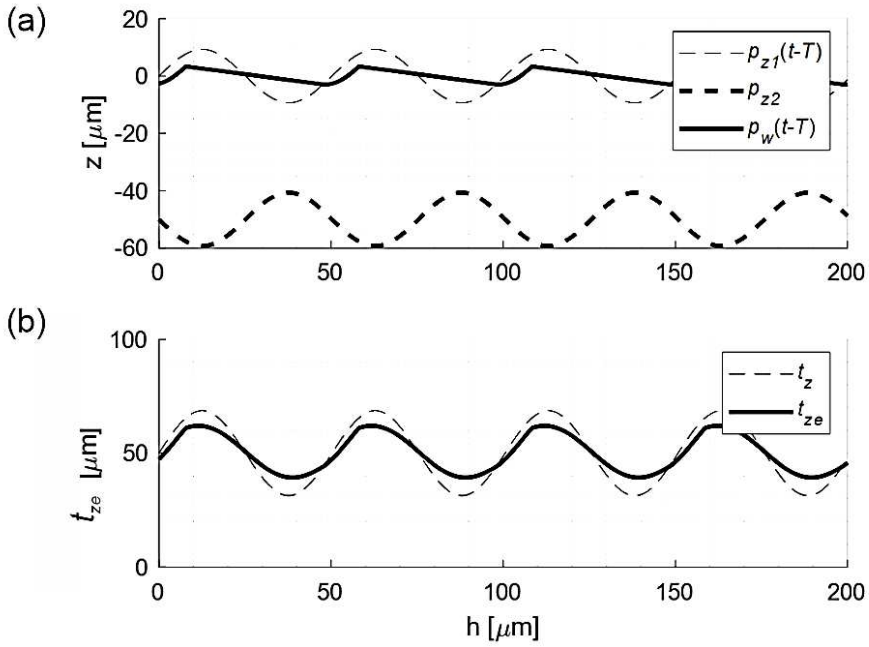


Figure 11. Uncut chip thickness variation comparison illustrating differences on the effective uncut chip thickness under certain parameters (r = 3 mm; S = 4000 rpm; f_o = 25000 Hz; A_o = 9.3 μm; γ = 9°;t_{z0} = 0.05 μm; v_t = 75 m/min; V_z = 141 m/min). (a) cutting trajectory of the successive cut under certain phase angle. (b) corresponding uncut chip thickness.

4. Finite element analysis of conventional and ultrasonic vibration-assisted drilling

This section describes the finite element analysis to explain the drilling performance improvement in UVAD. The analysis includes the comparison between the CD and UVAD at the elemental cutting-edge level. This allows the chip formation, stresses, cutting forces, and chip breakage to be captured in detail. The mechanisms which are expected to influence the performance are observed and analyzed.

4.1 Tool-workpiece interaction and chip formation

The tool-workpiece interaction in the along the whole drill bit geometry is known to be quite complicated. This section describes how the material being removed and chips are formed considering all the aspects that have been discussed in the previous sections. This helps the simplification or idealization stage in the FEA and ensure correct modelling techniques used.

In general, the material removal and chip formation in drilling process near the cutting edge can be illustrated in Figure 12. The difference in cutting velocity along the cutting edge and the geometry of the drill results in the

chip curling process after the material is removed [92]. Under this formation, the material is being cut and compressed so that different drilling parameters may result in different curling processes [69–71].

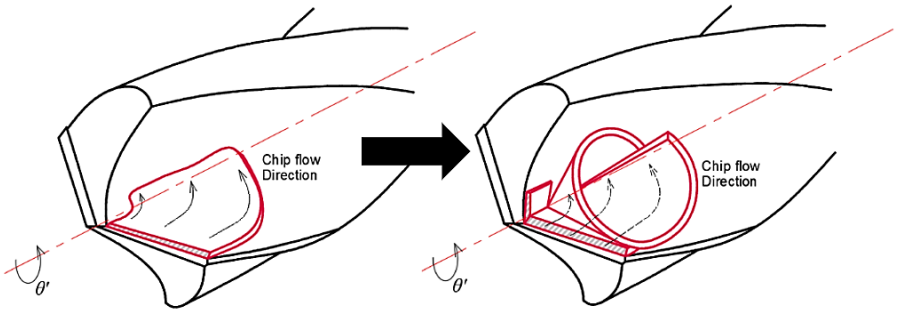


Figure 12. Chip formation on the drilling groove

Considering the t_{ze} and tool edge geometry, the cutting processes in FEA of CD and UVAD on a cutting point are depicted in Figure 13. In CD, the tool removes the material that follows t_{z0}. The material in the free surface is compressed while the back surface is burnished by the rake face of the tool. The machined surface profile is expected to not have the distinct profile for CD. In contrast to UVAD, the tool cuts and removes the material while following the cutting trajectory so the saw-tooth like surface profile is generated which means follows t_{ze}. This aspect is often neglected in several studies that discuss UVAM or UVAD [93]. The uncut chip thickness follows t_{ze} and the current cutting trajectory is influenced by the loading effect. In the free surface, the oscillation trace is found and expected to have a shorter λ_o due to the compression process. Meanwhile, oscillation trace in the back surface may be burnished by the rake face.

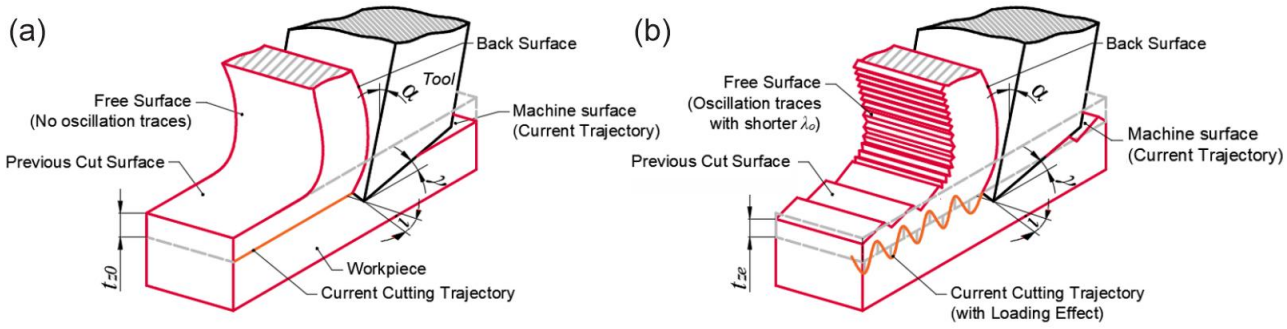


Figure 13. Cutting process in cutting point illustrating the differences of the chip formation. (a) In CD, and (b) In UVAD whereas the saw-tooth like profile and cutting point trajectory affects the chip formation

Note that oscillations do not only happen in the cutting edge but also the whole rake face and the drilling groove. It is expected that the formed chip near the cutting edge is influenced by the motion of the rake face as shown in Figure 14. Even though the cutting edge is not completely disengaged with the workpiece, the chip near the cutting edge is being moved back and forth at a very high frequency, thus it improves the chip breakage. On the other hand, it is also expected that the contact time between the chip and the drilling groove is reduced so that the friction is lower [68] while the oscillation motion also helps the chip to be evacuated from the drilling groove.

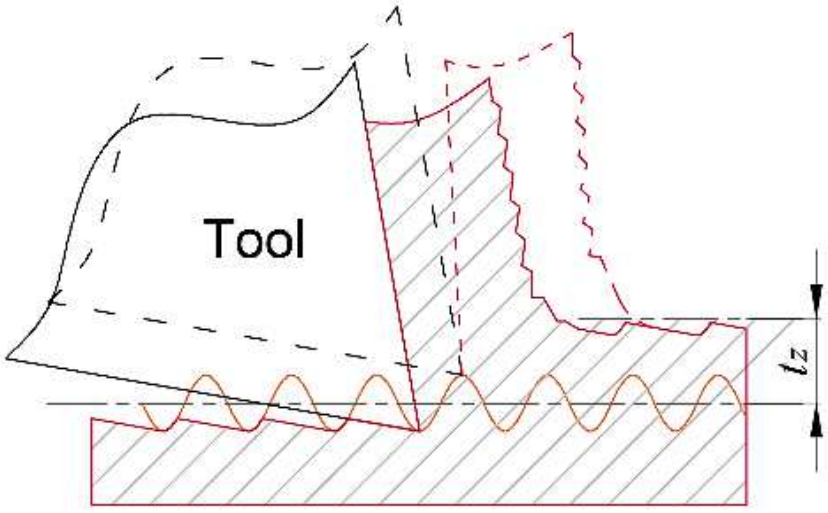


Figure 14. The effect of oscillation motion on the formed chip near the cutting edge

4.2 Finite element modelling and results

This section focuses on the technical details and settings used in the FEA model. The verification through the mesh convergence is also done to ensure that the FEA model is correct. The results show insights into several cutting mechanisms that promote improvement in the UVAD compared with CD.

4.2.1 Idealization

The idealization is considered to simplify and properly observe the details that happened in micrometer scale. This study used the derivation as shown in Section 2.1 to approximate the oblique cutting model into orthogonal cutting model as shown in Figure 13 and Figure 14. The elemental cutting edge used is positioned at r = 2 mm. A 2D plain strain is used because the elemental cutting edge is regarded as a very small cutting point on the cutting edge. The cutting parameters are considered constant throughout the cutting process. The well lubricated assumption is used so that the thermal influence is negligible.

4.2.2 Geometry models

Based on the derivations in the previous section, the cutting parameters used to define the FEA model in Abaqus Explicit Dynamics are shown in Table 2.

The geometry models of the cutting tool, workpiece, and the assembly are shown in Figure 15. The workpiece is modelled as rectangular, having 400x1000 μm. Each geometry is assembled so that the undeformed chip thickness tz_o as designated. Note that the workpiece geometry is split into two parts (top and bottom part) so that mesh size can be specified for each part.

Table 2. Cutting parameters correspond to observed elemental cutting edge.

Parameters	Value	Unit
Elemental radius (r)	2	mm
Cutting speed ($V_f(r)$)	0.209	m/s
Uncut chip thickness (tz_o)	50	μm
Rake angle (α)	23.728°	degree
Clearence angle (γ)	5°	degree
Amplitude (A_o)	16.21	μm
Frequency (f_o)	20,000	Hz

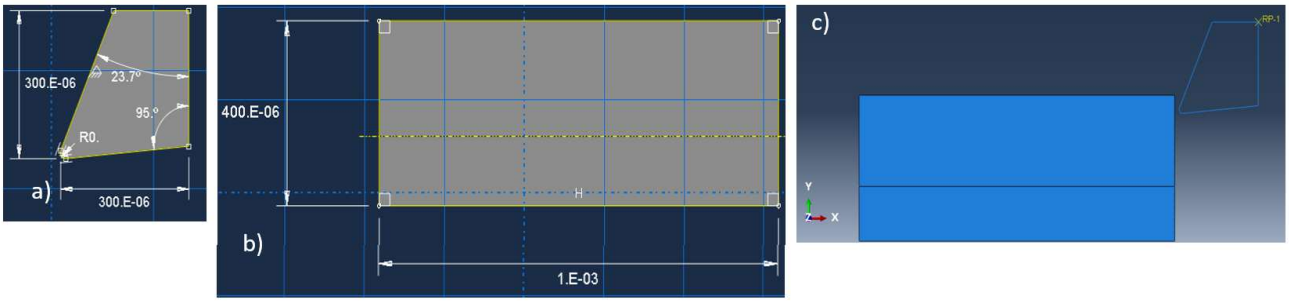


Figure 15. Geometry models required in FEA to model UVAD.
(a) cutting tool model (rigid). (b) workpiece model (flexible). (c) assembly

4.2.3 Material properties

Analytical rigid setting is applied on the tool so that in assembly it is shown as line where no material property needed, and no mesh needed to apply. The tool is assumed to be rigid throughout the simulation such that no deformation occurs. On contrary, the material properties of AL6061-T6 are applied on the workpiece geometry. The properties are density, elasticity, Johnson-Cook (JC) strength model, and JC damage model [94]. The JC strength model is shown to be:

$$\sigma = (A + B\varepsilon^n)(1 + C\ln\dot{\varepsilon})\left[1 - \left(\frac{T - T_{room}}{T_m - T_{room}}\right)^m\right] \quad (20)$$

Where the first term corresponds to yield stress and strain hardening behavior, the second term corresponds to the strain-rate dependent behavior, and last term is the thermal dependent behavior of the material. Moreover, the resulting true stress-strain of AL6061 is depicted in Figure 16.

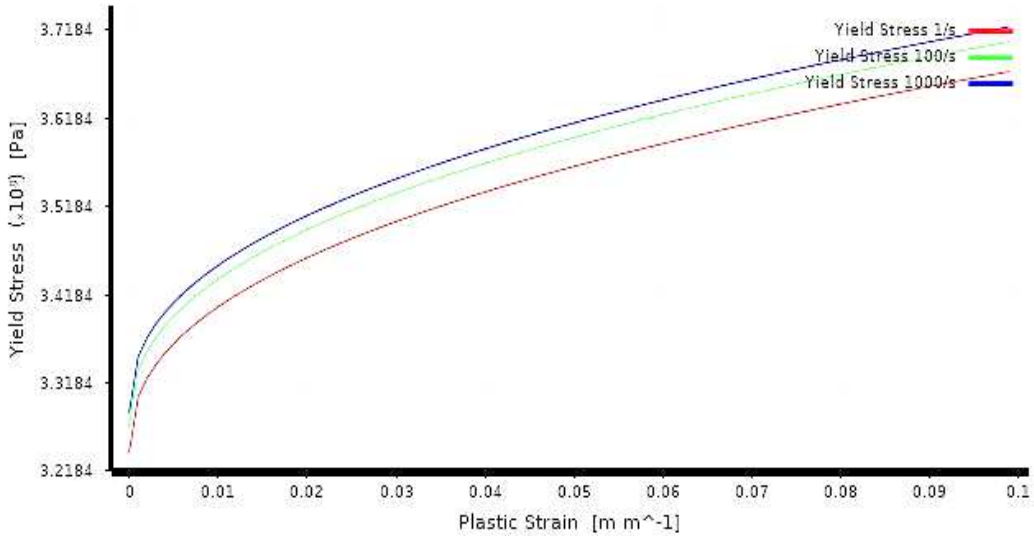


Figure 16. Yield stress-plastic strain plot obtained from Johnson-Cook strength model which also demonstrates the effect of strain rate on the stress-strain curve

The JC failure model determines the point of material fracture $\bar{\varepsilon}_f$ by considering the decoupled factors which are stress triaxiality, strain rate, and temperature, which are defined as:

$$\bar{\varepsilon}_f = \left[D_1 + D_2 e^{D_3 \sigma^*}\right][1 + D_4 \varepsilon^*][1 + D_5 T^*]. \quad (21)$$

Stress triaxiality is represented by the material-specific constants D_1, D_2, and D_3. The variable σ^* represents the triaxiality ration calculated as the average normal stress divided by the von-Mises equivalent stress [95]. The strain rate effects are determined by the material-specific constant D_4 and dimensionless strain rate ratio ε^* which compares the viscoelastic strain rate to a reference strain rate [95]. Moreover, the thermal softening is accounted through the material-specific constant D_5 and homologous temperature of the material T^* [95].

The overall damage within the material is expressed by damage criterion D which is defined as summation of equivalent plastic strain increments $\Delta\bar{\varepsilon}_p$ relative to the calculated fracture strain $\bar{\varepsilon}_f$ as follows:

$$D = \sum \frac{\Delta\bar{\varepsilon}_p}{\bar{\varepsilon}_f} \ . \quad (22)$$

The model assumes that the damage begins as soon as the viscoplasticity occurs. The D value of 0 means the material is undamaged until it reaches the value of 1 that represents the material is fully damaged thus failure occurs [94,95]. The parameters and their corresponding value used in this FEA are listed in Table 3.

Table 3. Parameters used in material models

Parameter	Value	Parameter	Value
General		**Johnson-Cook Damage**	
Density, ρ	2700 kg/m³	Material-specific Constant, D_1	-0.77
Elasticity		Material-specific Constant, D_2	1.45
Young's Modulus, E	68.9 GPa	Material-specific Constant, D_3	-0.47
Poisson's Ratio, γ	0.25	Material-specific Constant, D_4	0
		Material-specific Constant, D_5	1.6

Johnson-Cook Strength			
Yield Stress, A	324 MPa	Strain Hardening Exponent, n	0.42
Strain Hardening Parameter, B	114 MPa	Melting Temperature, T_m	925 K
Strain Rate Parameter, C	0.002	Room Temperature, T_{room}	300 K
Thermal Softening Exponent, m	1.34	Reference strain rate, ε_{ref}	1/s

4.2.4 Boundary conditions

The boundary conditions are based on the condition applied on elemental cutting point as discussed in the idealization. It is depicted in Figure 17 where these boundary conditions are designated to model the cutting process in UVAD.

The bottom edge of the bottom part of workpiece is fixed to restrict all the displacements and rotations. Meanwhile, the tool as target surface and top part of the workpiece as contact surface are determined in the surface-to-surface contact with the coefficient of friction μ of 0.3.

On the tool body, the reference point (RP-1) is created as a pilot to control the motion of the tool that follows the cutting trajectory as in kinematics. The displacement boundary condition which restricts the tool displacement and rotation along the z-axis is applied on this reference point. Moreover, the velocity is applied on it to represent the V_t of 0.209 m/s on negative x-axis direction. Only for the FEA of UVAD, the periodic amplitude is applied on the reference point to have oscillatory motion with A_o of 16.21 μm and f_o of 20 kHz to model the existence of ultrasonic vibration support. Therefore, no load or force are applied on the analysis. On the other hand, the reaction forces on the reference point will be gathered and regarded as cutting forces occurred.

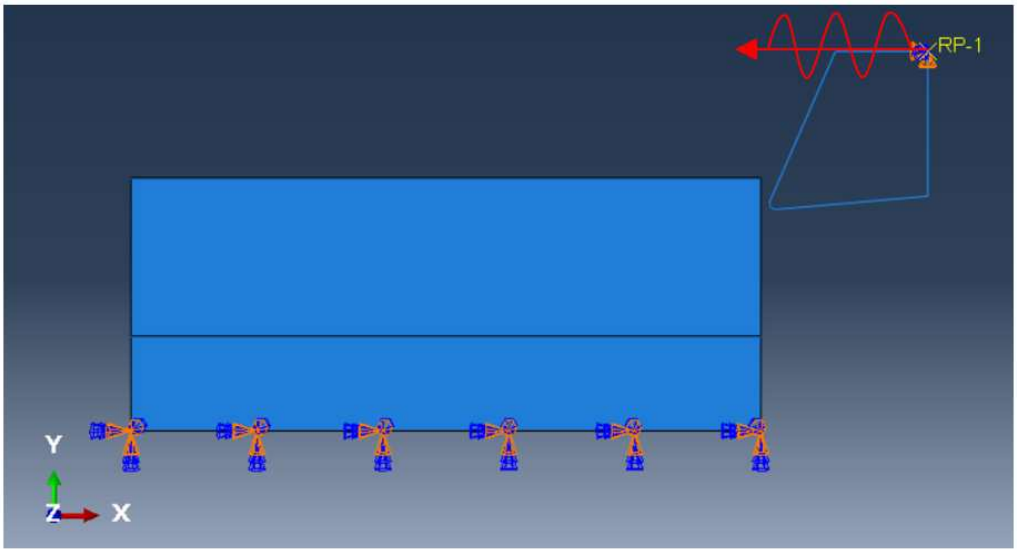


Figure 17. Boundary conditions applied including the fixed on the workpiece and cutting trajectory constraint on the tool

4.2.5 Discretization

Discretization is performed only on the workpiece as shown in Figure 18, while the analytical rigid bodies (tool) do not need to be meshed. The mesh size on the cutting area (top part of the workpiece) is 5 μm while the other part is 10 μm. The Arbitrary-Langlarian-Eulerian (ALE) adaptive mesh is set to the mesh so that the large distortion issue could be anticipated as shown in Figure 19 [96]. Moreover, the element type used is explicit with element deletion is turned on so that the damage model is working.

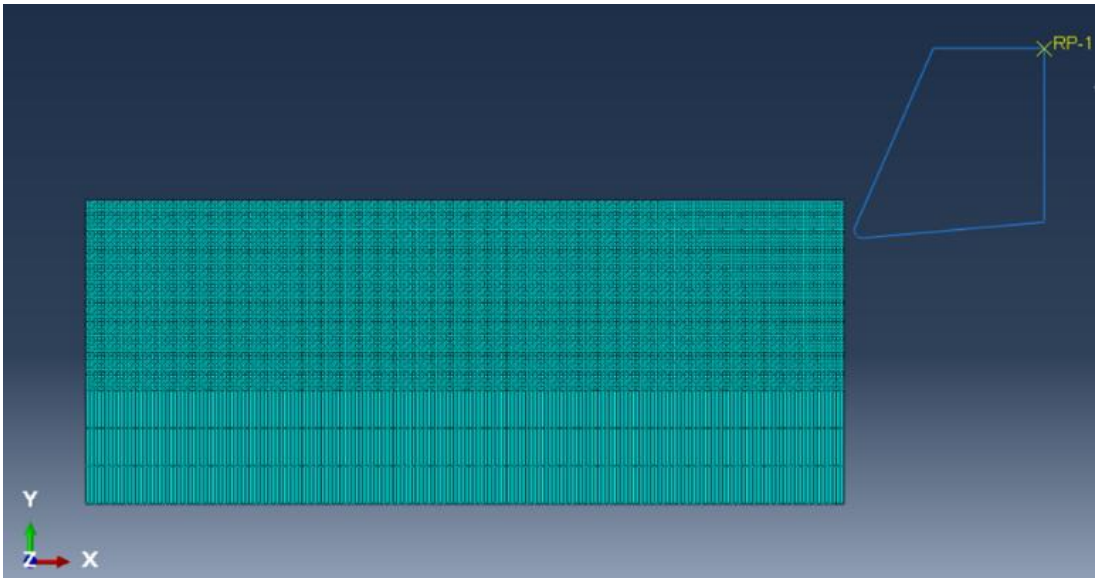


Figure 18. Discretization of geometries model in the FEA with smallest mesh size at 5 μm

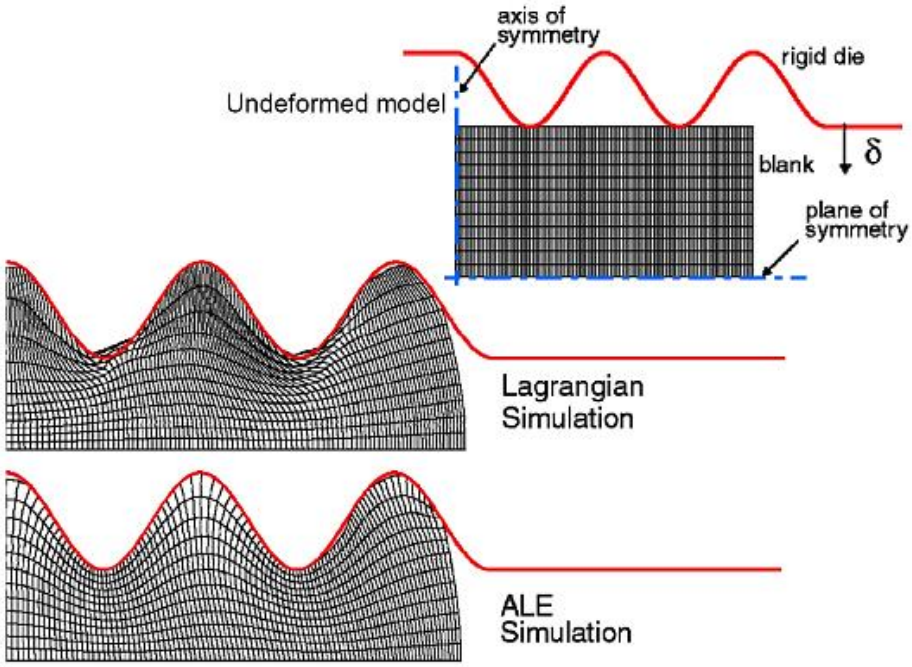


Figure 19. Illustration of the ALE adaptive mesh effect on the simulation on handling the deformation under complex profile compression [96]

4.2.6 Analysis settings and solving process

Some adjustments in the analysis settings are made beforehand as follows:

a. The period of the analysis is set to be 4 x 10^{-3} s.

b. Total of 19,886,709 increments for 100 step intervals performed.

c. The time step settings are set to be default.

d. Field output request of the status (VUMAT) is checked to be able get failure and plasticity models output values.

e. Mass scaling is turned off to obtain accurate results with longer computational time as consequence.

f. The frame-interval is set to be 100 so that more data points can be obtained so that higher frame rate and smoother animation during the post processing.

4.2.7 Finite element analysis results

The experimental result is used to validate the accuracy of the FEA result. The verified mechanistic model of CD [97] is used to obtain comparable elemental cutting force with the parameters mentioned in Table 1. The flowchart to obtain the elemental cutting force is shown in Figure 20. The model is based on the drill bit geometry analysis, Johnson-Cook Strength model, oblique cutting model with shearing and ploughing mechanism [97]. Besides the input that is shown, the cross-sectional chip thickness is submitted into the mechanistic model. A cutting edge on 6 mm drill bit is divided into 5000 cutting elements and particular elements at radius of 2 mm is obtained. The mechanistic model provides the resultant cutting force per unit width which is specific on the cutting point. Figure 21 shows the tangential (*Ft*), radial (*Fr*), axial (*Fa*), and resultant cutting forces (*Fc*) per unit width for the cutting points along the cutting edge of the drill bit.

The F_c of the cutting element obtained from the experiment and analyzed through mechanistic model (labelled as '*exp*') is shown along with the numerical results in Figure 22 with the value of 33,518 N/m. The moving average (bold lines) are obtained from the reaction forces (dotted lines) in the CD FEA with different mesh sizes. The cutting force is converged as the mesh size decreases. The force of 5 μm mesh size analysis hit the plateau at around 32,000 N/m where it is quite agreeing. The error is considered acceptable as the approximation into the orthogonal cutting process is used in this study. Moreover, the contributing factor that influences the difference is the fact that the chip formation is hindered by the drill groove and generated hole thus chip evacuation force occurs [67,83]. Considering the computational cost is very higher for smaller mesh sizes, the 5 μm mesh size is reasonable option to be used in this study.

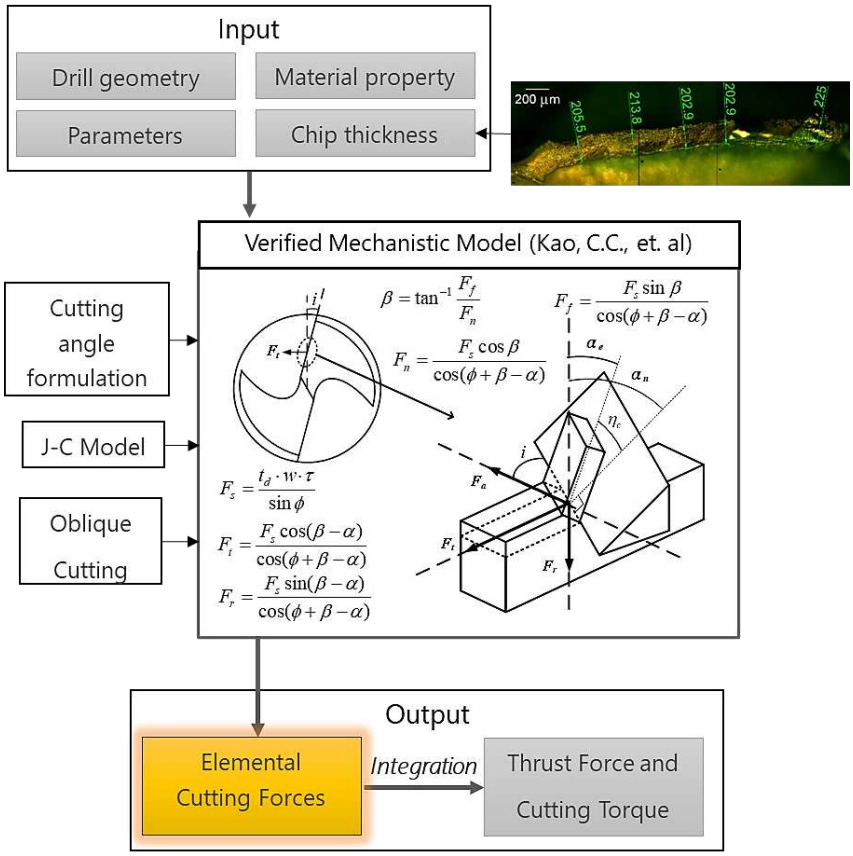


Figure 20. Flowchart for the elemental cutting force validation from measured chip thickness in experiment which analyzed by mechanistic models to obtain elemental cutting force

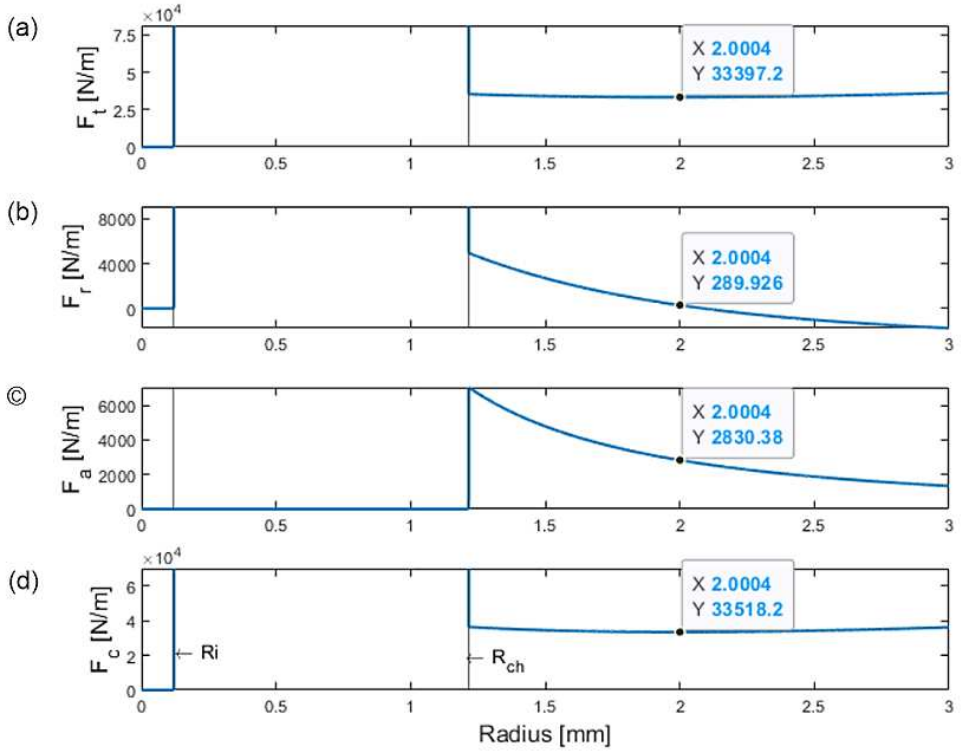


Figure 21. The elemental cutting forces (per unit width) in all directions from the experiment analyzed with mechanistic model along the radius (data point is at r = 2 mm). (a) tangential (F_t), (b) radial / transversal (F_r), (c) axial (F_a), (d) resultant (F_c)

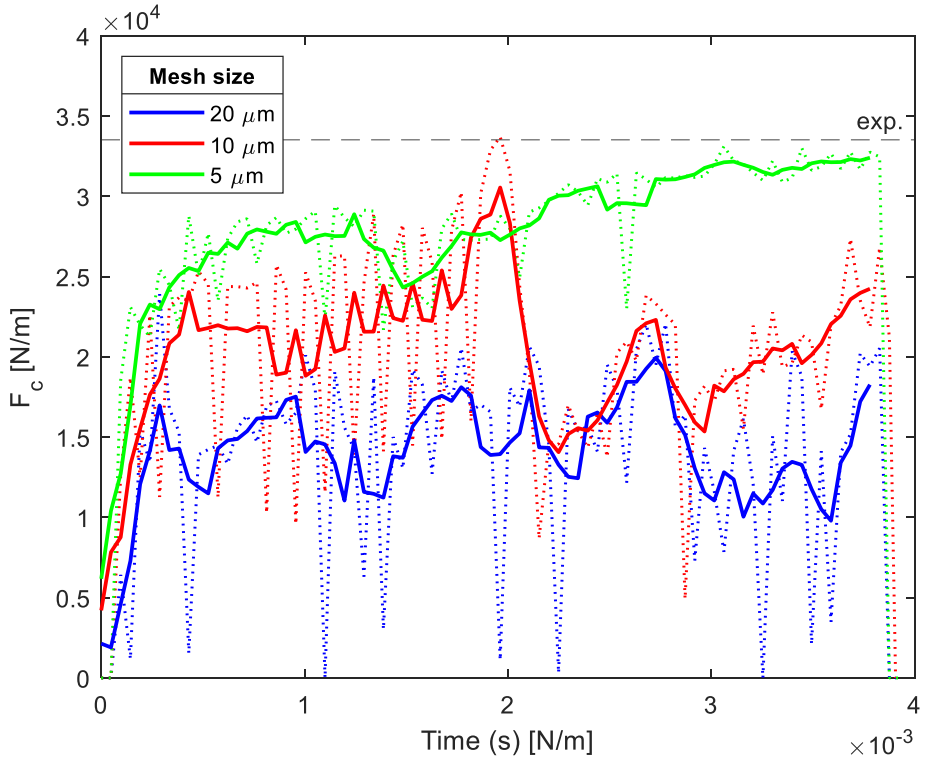


Figure 22. Resultant cutting force for different mesh sizes and expected value from mechanistic model (experimental result). It is shown that the mesh size of 5 μm is sufficient and converged

The analysis is performed to show the equivalent stress distribution for both CD and UVAD. General observation in the timeline is shown in Figure 23 while more detailed plots with smaller time steps are shown in Figure A.3 at Appendix A. The cutting tool moves following the motion on each type of drilling (CD or UVAD). Note that the first chip breaks in UVAD at 0.001723 seconds while in long chip is created in CD.

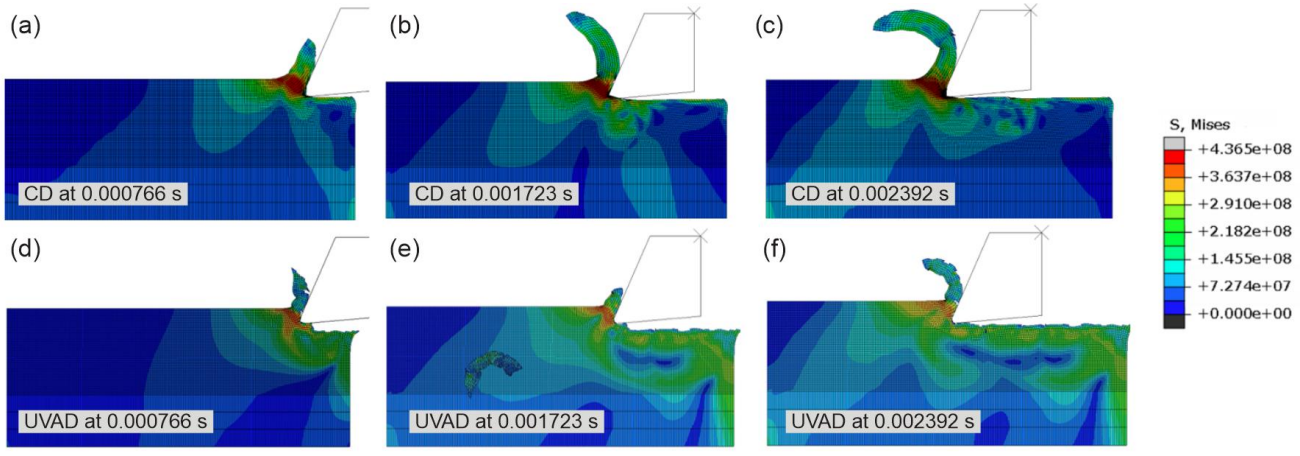


Figure 23. The finite element analysis results (von-misses stress distribution) comparison. For CD at (a) 0.000766, (b) 0.001723, (c) 0.002392 seconds. For UVAD at (d) 0.000766, (e) 0.001723, (f) 0.002392 seconds.

a. Cutting forces

The nodal reaction force is requested to be shown in the post processor that it can be used as comparison indicators between CD and UVAD. The cutting forces, which are F_c, F_t, and F_r, can be seen in Figure 24. The F_r

and F_t cutting force of UVM is lower compared to them in CD. The negative value in tangential force is due to the coordinate system (x positive to the right). Meanwhile, the F_r of UVAD is slightly higher compared with the UVAD due to penetration upon tool that moving down along oscillation. This is to show that UVAD promotes lower cutting force around 33% reduction at the elemental level and to be accumulated if the whole cutting-edge length is considered. The underlining phenomena that promote the cutting force reduction and drilling improvements are discussed in the following sections.

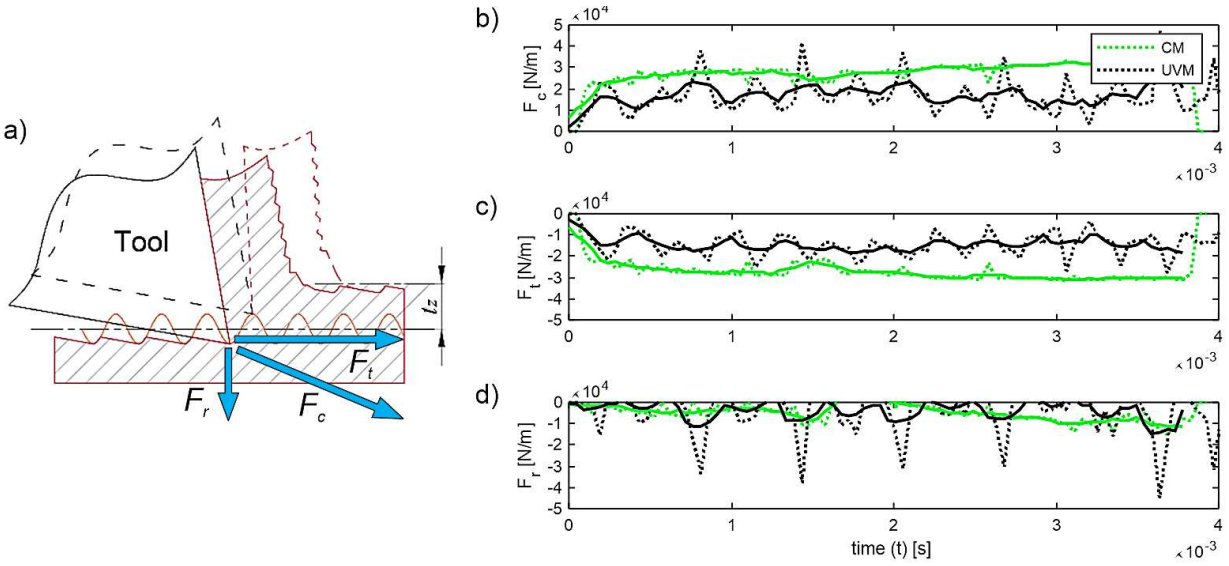


Figure 24. Cutting forces comparison between CD and UVAD.
(a) Cutting forces direction, (b) tangential (F_t), (c) transversal (F_r), (d) resultant (F_c). The figures indicate that the cutting forces are lower in UVAD except for there are force peaks in radial direction resulted from tool penetration in the direction

b. Altering effective rake angle and contact length during oscillation

Several references pointed out that the effective rake angle (α_e) is defined by measuring the imaginary line which is perpendicular to the cutting velocity direction to the surface of the rake face as shown in Figure 25. Based on this definition, the effective rake angle is constantly changing along with the progress of oscillation causing different modes of cutting to occur alternatively at high frequency in UVAD as also depicted in Figure 25. In CD, the α_e is found to be the same as the tool rake angle (α). In UVAD, when the α_e is negative, the grinding-like mechanism persists while the α_e is positive, the cutting mechanism that occurs. The angle is measured to vary between a minimum negative α_e of -6° to the maximum positive α_e of 148°. The primary shear zone equivalent stress value is varying along the oscillation progression. This is to show that different mechanisms occur in UVAD. Moreover, this mechanism influences the chip formation and breaking as discussed in the following section. This mechanism also agrees with results from Yin et al. [98] where the vibration assistance promotes plastic material removal and increases material plasticity. This mechanism is also termed as acoustic softening effect as discussed by Cui et al. [99] and Wang et al. [100].

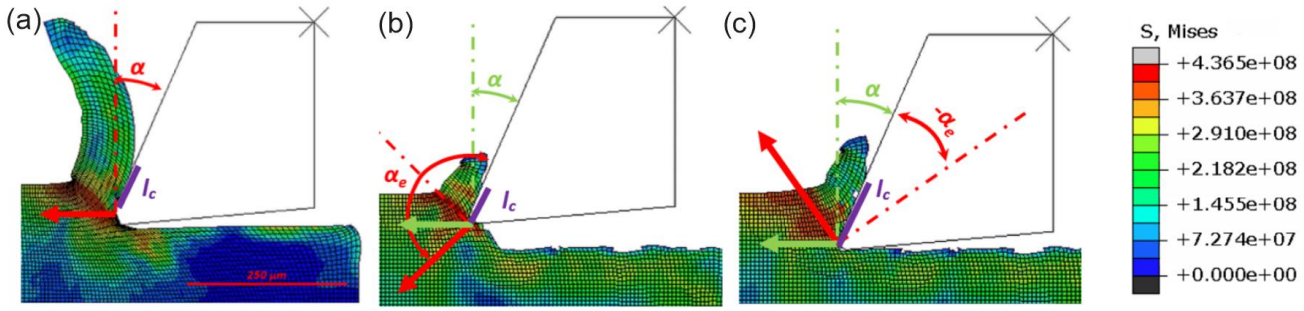


Figure 25. The illustration of measured effective rake angle α_e and contact length l_c and its variations, (a) in CD (constant), (b) in UVAD (tool going down, positive max α_e), (c) in UVAD (tool going up, negative min α_e)

The effective contact length is measured in both CD and UVAD as illustrated in Figure 25. From the comprehensive observation, the contact length is consistent all the time with 90 μm in CD, while the contact length is varying between 41 μm to 107 μm in UVAD at high frequency. The contact length is closely related to the second deformation zone and friction between rake face and generated chips [101]. This is a possible reason that promotes better tool life, as discussed in many references [13,17,24,26,98,102], where the chip is easier to evacuate upon the tool moving up along the oscillation.

c. Chip formation and topology analysis

As mentioned before, the chip is easier to evacuate when the tool is moving up thus affecting the chip formation mechanism. It can be seen in Figure 26 that there is higher curvature in the free surface of UVAD chips compared with it in CD. Moreover, several micro fractures are found on the back surface which are created following the period of oscillation as also claimed in [44]. The curling radius is found to be smaller in UVAD with 66 μm compared with CM with 189 μm. In addition, the curling rate in UVAD is much higher as the chip curling angle is measured to be 224° compared with 73° in CD at the same time stamp. This indicates that UVAD promotes better chip breaking.

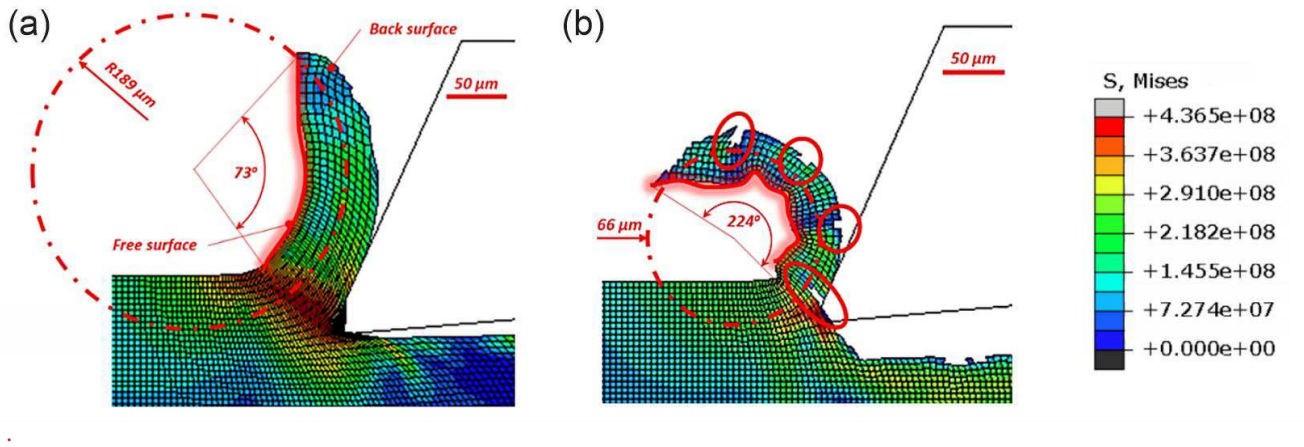


Figure 26. FEA results for chip formation and topology, (a) in CD (high curling radius, slow curling rate, no weak points occur), (b) UVAD (low curling radius, fast curling rate, weak points occur)

Figure 27 depicts the chip thickness measurement and variation along with its length. In general, UVAD gives thinner and shorter chips and more fluctuating along its length. The minimum chip thickness contributes as weak points where that promotes better chip breakage. Upon the chip contact or receiving any additional load during chip formation, the chip is expected to break. Note that at the same time stamp shown, the UVAD gives two chip breakage while CD gives none.

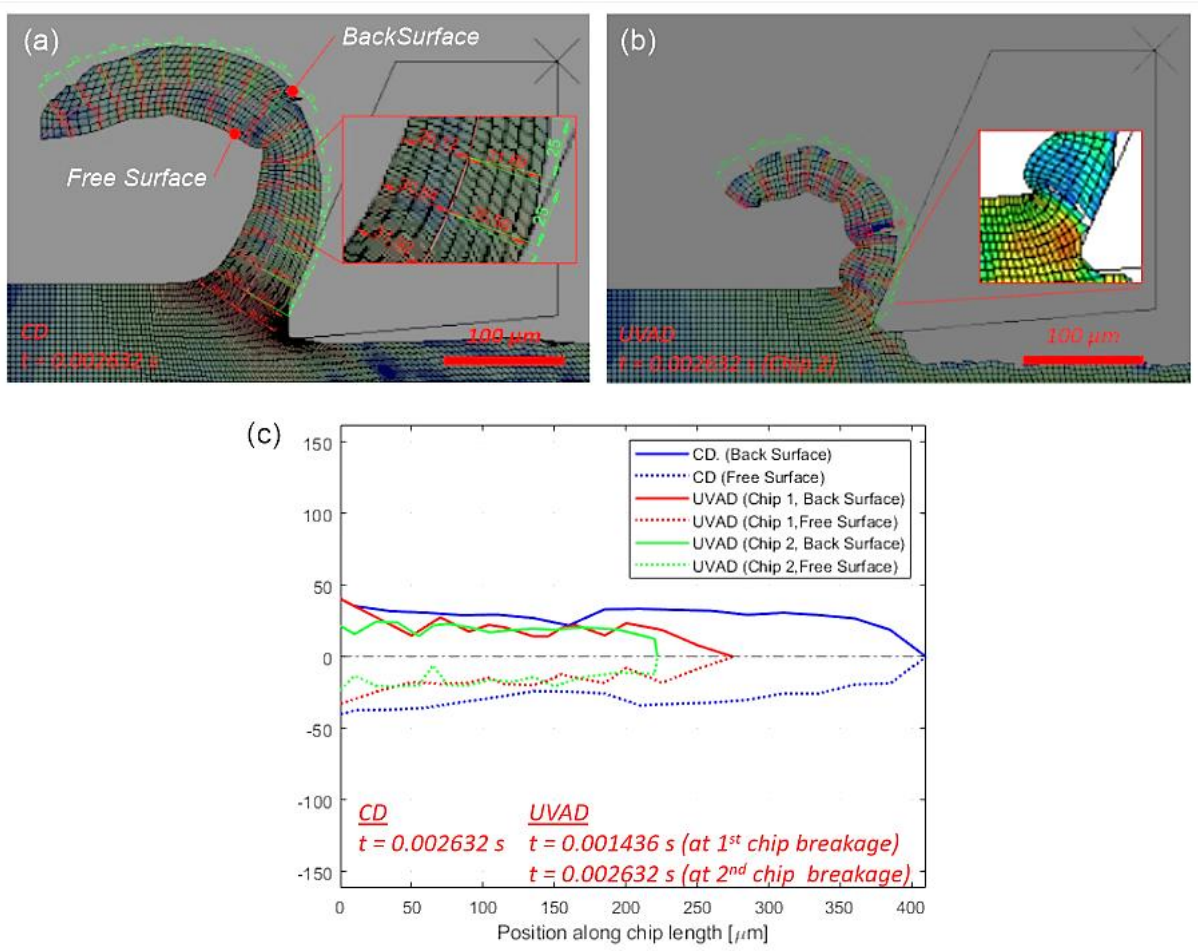


Figure 27. FEA results in chip thickness variation, for (a) in CD (thicker and longer chip), (b) UVAD (thinner and shorter chips with weak points), (c) measured chip thickness across two chip breakage times

d. Chip breakages

As stated in many literatures mentioned, UVAD gives better chip breakage performance compared with CD [17,24]. Over the whole simulation time, the chip breakage count is four as depicted as in Figure 28. The first chip breakage time is shown to be longer in UVAD because this is the transient phase as the tool initially cut. As the cutting progresses, the steadier the chip breakage becomes. This concludes the reason for chip breakage improvement in UVAD due to many factors discussed before.

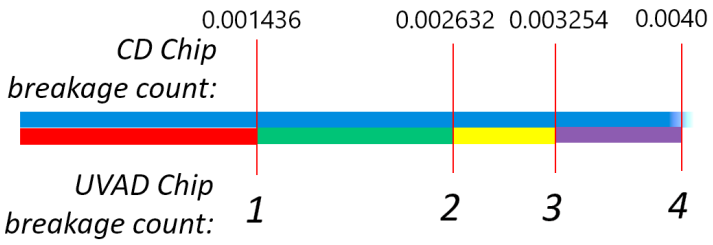


Figure 28. Chip breakage timeline in CD and UVAD which illustrate the UVAD has more breakage count throughout simulation

e. Machined surface topology with micro hammering effect

Figure 29 depicts the machined surface topology comparison. The CD gives flat topology while the UVAD gives distinct sawtooth-like profile. The penetration happened upon the oscillation causes the flank face to contact with the workpiece. It promotes even better chip breakage if the topology is on the intermediate surface such that it will be removed by the successive tool edge, and the topology accumulates in free surface of chip.

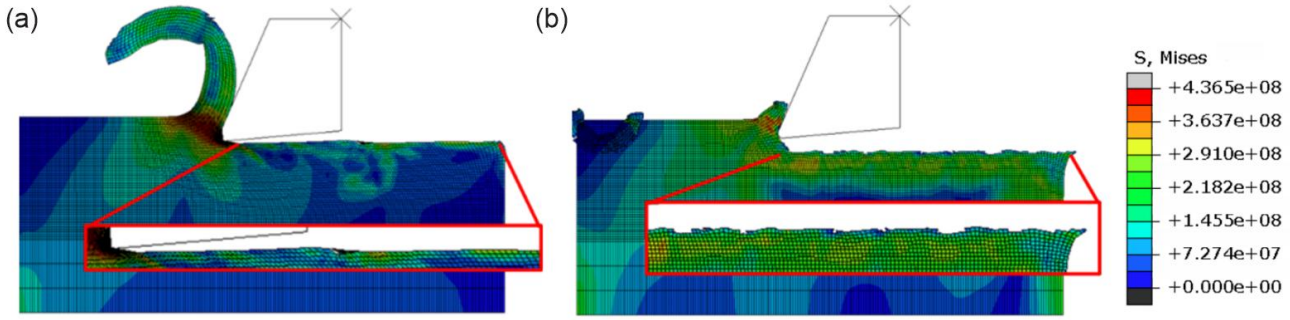


Figure 29. Machined surface topology from FEA, for
(a) CD (no distinct profile), and (b) UVAD (distinct profile promotes better chip formation in following cuts)

f. Workpiece subsurface

Figure 30 shows the residual stress found in the subsurface in the machining process. The residual stress in UVM has higher values which is around 225 MPa at 0-80 μm. The penetration motion is found to be main reason, and it is also supported by the cyclic and higher average transversal (radial) cutting force. Near the surface, the localized tensile stresses build up that promote micro-cracking which makes it easier for chips to break away. As intermediate surface, this part will be cut in the successive cut thus it expected to give better drilling performance. Further analysis should be done to precisely conclude this finding such as its effect on the subsurface such as in [103,104].

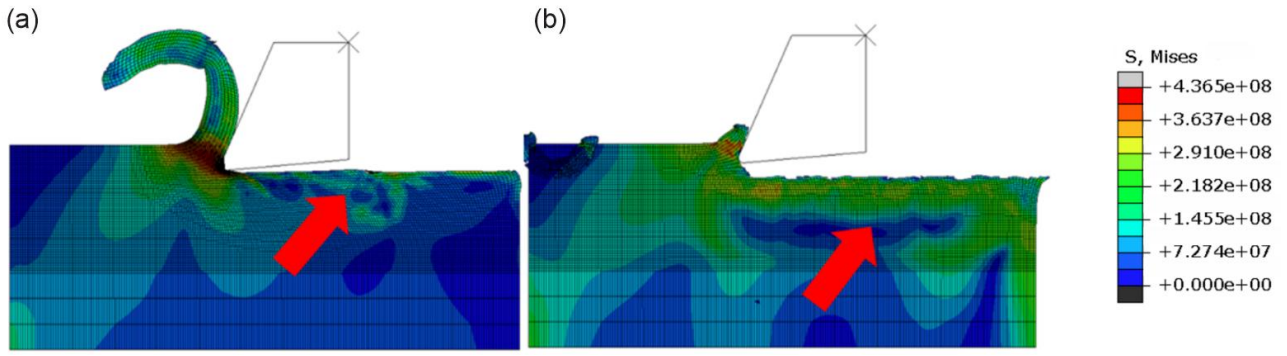


Figure 30. Residual stress on machined workpiece subsurface in
(a) CD (compression residual stresses), and (b) UVAD (compression residual stresses persists)

5. Experimental Result and Discussion

Based on studies in literature and FEA results, experimental studies are designated into two sections. The first section discusses UVAD with low feed per tooth to demonstrate whether the interrupted cutting trajectory truly occurring in UVAD as inferred in some of the literature. The second section focuses on the applicable feed per tooth which is commonly used upon deploying UVAD. The findings are correlated with the kinematics and FEA studies so that the insights are more explainable.

5.1 Ultrasonic vibration-assisted drilling experiment with low-feed per tooth

Some references claimed the importance of the interrupted cutting trajectories in UVAD resulting in discretized chip shape [72,73,75]. Meanwhile, the references show that the chips are not discretized within the corresponding λ_o as expected (which is in micron scale) as in the kinematics. Moreover, the low t_{z0} is required to get the interrupted cutting trajectories in UVAD. Even though it is not practical for industrial application, this section is presented to investigate whether the interrupted cutting trajectories in UVAD are important and the reason for the unexpected chip discretization.

The experiment configuration used in this section is shown in Table 4. The pre-hole drill diameter is considered to avoid the chisel edge effect on the drilling process thus the real actual cutting process on cutting lip can be observed.

Table 4. Low feed drilling experiment parameters

Exp. No.	Drilling parameters		Oscillation parameters		Pre-hole drill diameter [mm]	Drilling depth H [mm]	Average Forces	
	S [rpm]	t_{z0} [mm/ tooth]	A_o [μm]	f_o [μm]			F_z [N]	T_z [Nm]
CDA	3000	0.005	-	-	-	5	51.8	0.18
VDA	3000	0.005	16.2	25000	-		52.00	0.20
CDB	3000	0.005	-	-	3		1.54	0.11
VDB	3000	0.005	16.2	25000	3		3.30	0.10

Based on the drilling and oscillation parameters, the initial cutting trajectories that consider the micro hammering effect are shown in Figure 31. The phase lag (ϕ_{lag}) is set to be 180^0 to maximize the chip breakage. The tool separation t_{ze} reaches the negative value up to -13.94 μm. This means that the tool edge is disengaged from the wiped surface profile up to this distance in very high frequency. Moreover, the expected length of the chips is 23.18 μm.

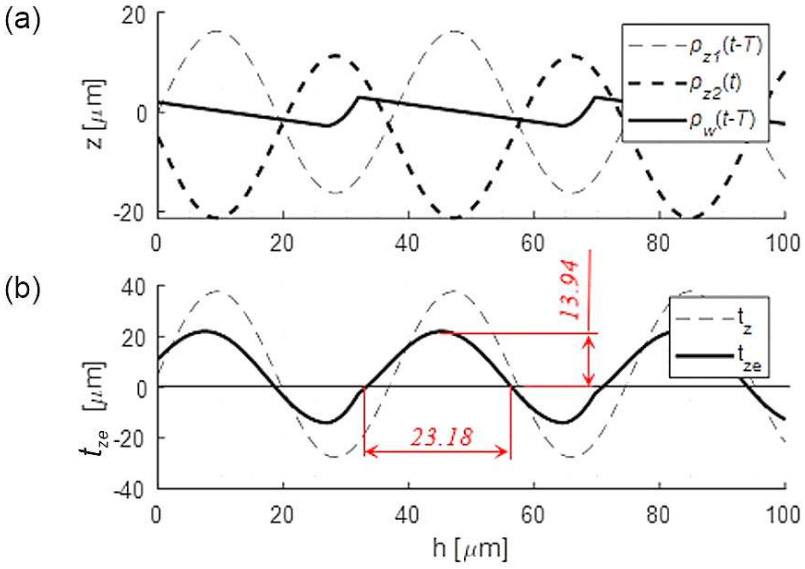


Figure 31. Effective Uncut chip thickness variation in low-feed drilling experiment in UVAD indicating complete tool-workpiece separation that creates interrupted cut under certain parameters (V_t = 56.52 m/min; H_w = 5.73 μm; λ_o = 37.70 μm; L_w = 32.50 μm; ϕ_{lag} = 180^0). (a) cutting trajectory of the successive cut under certain phase angle, (b) corresponding uncut chip thickness

The chip shapes for these experiments can be observed in Figure 32. The shapes vary starting from needle chips, flake chips, spiral chips, and long chips for CDA and VDA. It is expected that the long chip resulted from extrusion in chisel edge which is found in the non-pre-hole drilling. In CDB and VDB, the chips are more discretized even though the chip length is still not as short as expected within micron scale. The chips are composed of needles, flakes and spiral shapes. Overall, it shows that UVAD gives better chip breakage.

The disengagement of the tool is at 13.94 μm which happened at a very high frequency (around 25 kHz). Due to small disengagement at high frequency and the loading effect that reduces the effective amplitude during the cutting progression, the chips shown in Figure 33 are not discretized as in the cutting trajectory. However, any oscillation traces might be able to be seen in the topology of the chip, so the observation of the chips in this experiment is performed. Similar chip shapes for UVAD were also observed in a study by Duman et al. [74].

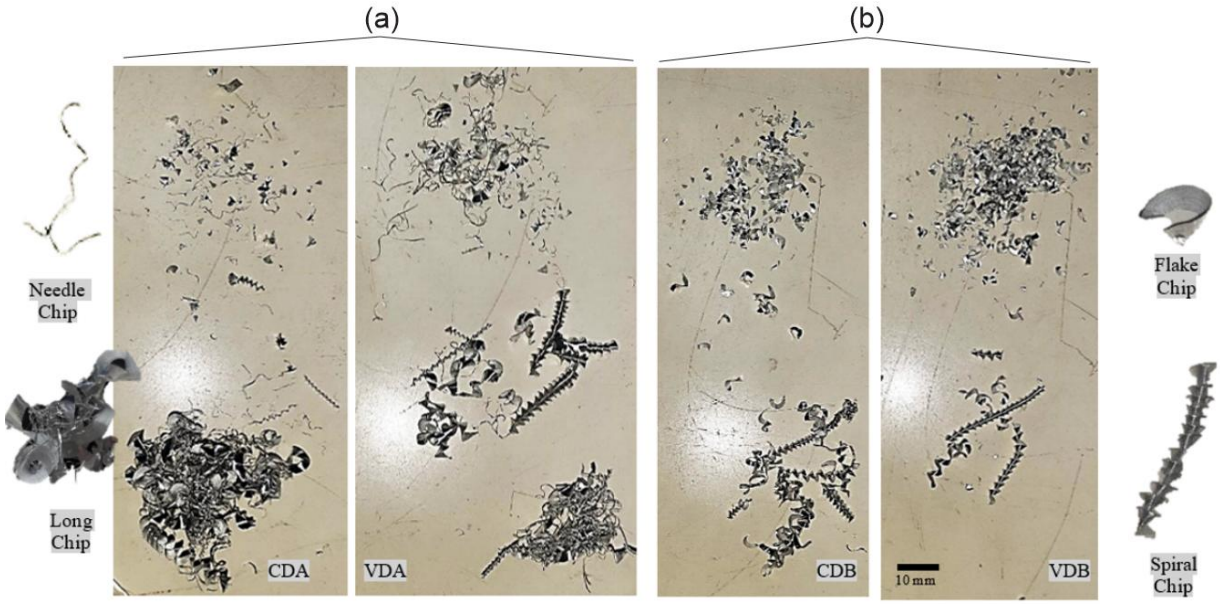


Figure 32. Chip shapes in low feed drilling experiments show no discretization in micron level as in simulated effective chip thickness. (a) without pre-hole, (b) with pre-hole

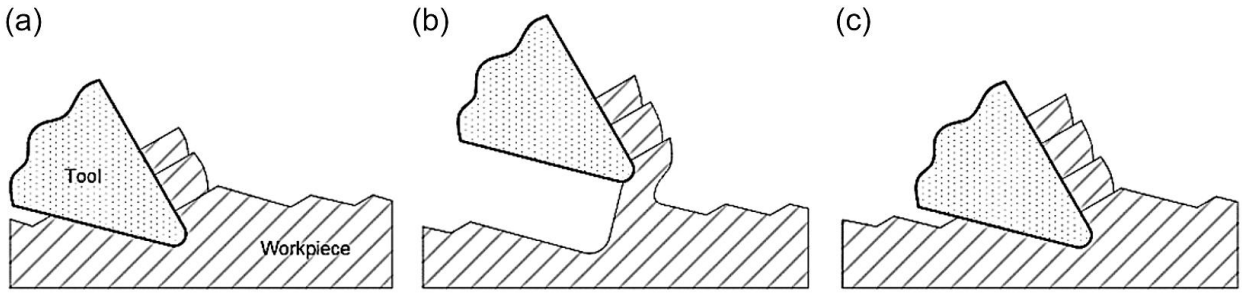


Figure 33. illustration on the tool separation does not occur in low-feed drilling experiments due to loading effect and ductile stickiness

The spiral chip topology is observed further for the low-feed drilling chips. Figure 34 depicts the microscope observation of the spiral chip from CDA and VDA. In this experiment number, the higher loading condition occurred compared with CDB and VDB that will be observed later. The oscillation traces are found only on the free surface of the chip from VDA. Moreover, the chip thickness in VDA does not have many variations as shown in the peripheral direction.

Figure 35 shows the chip topology for CDB and VDB that have lower loading conditions. The oscillation traces are found in both the free and back surfaces of the chip from VDB. This is to signify the significance of the phase lag effect as both sides of the chip have oscillation traces when the chip is thin. More variation of chip thickness also appears in VDB as shown in the peripheral direction. The reasons for this are the low feed per tooth and the A_{oe} for this experiment is higher compared to VDA. Besides, there are also jagged edges at the peripheral of the drilling chips as pointed out in Figure 35 which is expected due to non-uniform chip deformation because of the

high variation of the chip thickness. It is shown that there are critical chip thicknesses as the location for easier chip breakage.

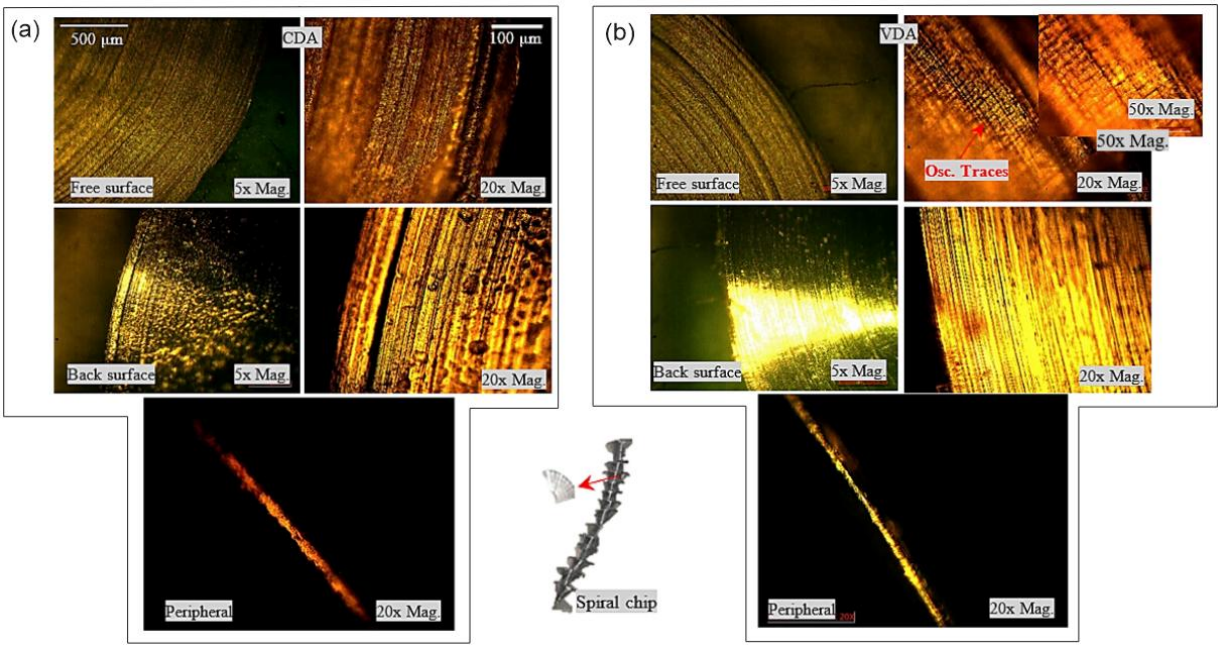


Figure 34. The spiral chip topology and thickness in experiment number (a) CDA, and (b) VDA which shows distinct surface profile on the free surface in VDA

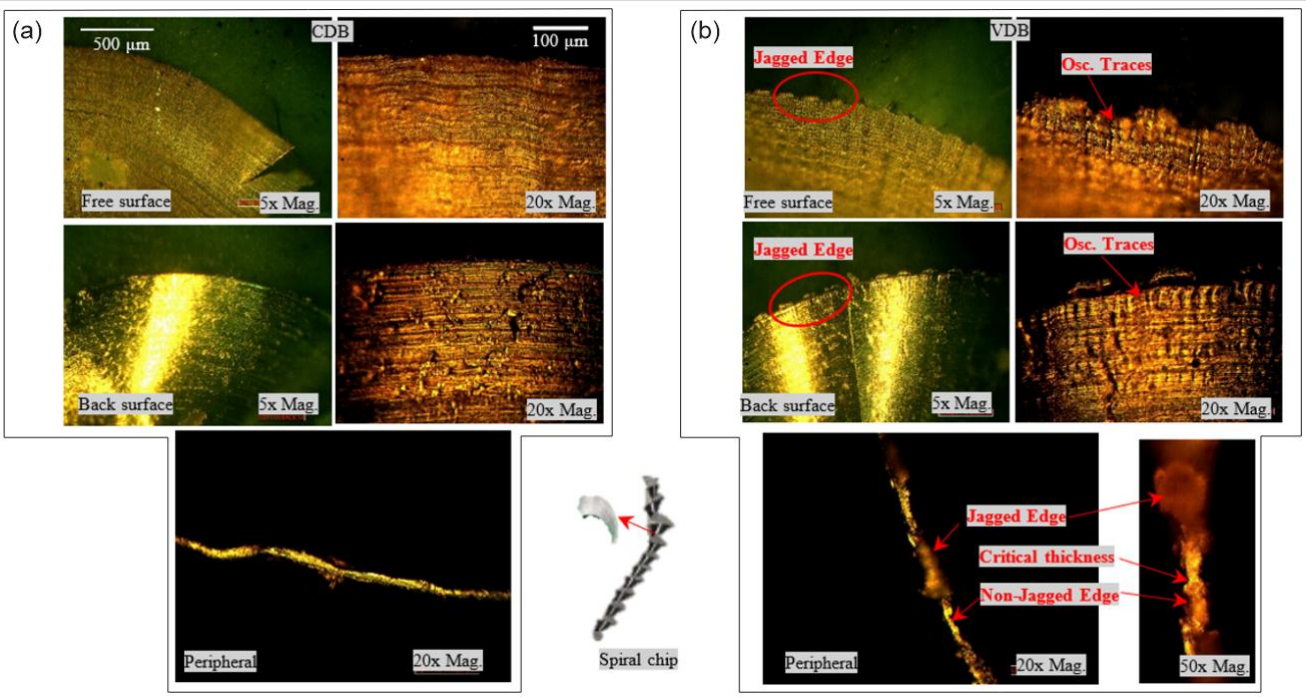


Figure 35. The spiral chip topology and thickness in experiment number (a) CDB, and (b) VDB which shows distinct surface profile on the free surface in VDB

Moreover, the same observation is performed in the smaller and shorter chip, which is the flake chip, from VDB as shown in Figure 36. More distinct effects of oscillation traces and phase lag occur. Oscillation traces, jagged

edges, and critical thickness are found to be more distinct. The oscillation traces in both free and back surfaces also the presence of critical thickness signifies the phase lag effect in low-feed drilling.

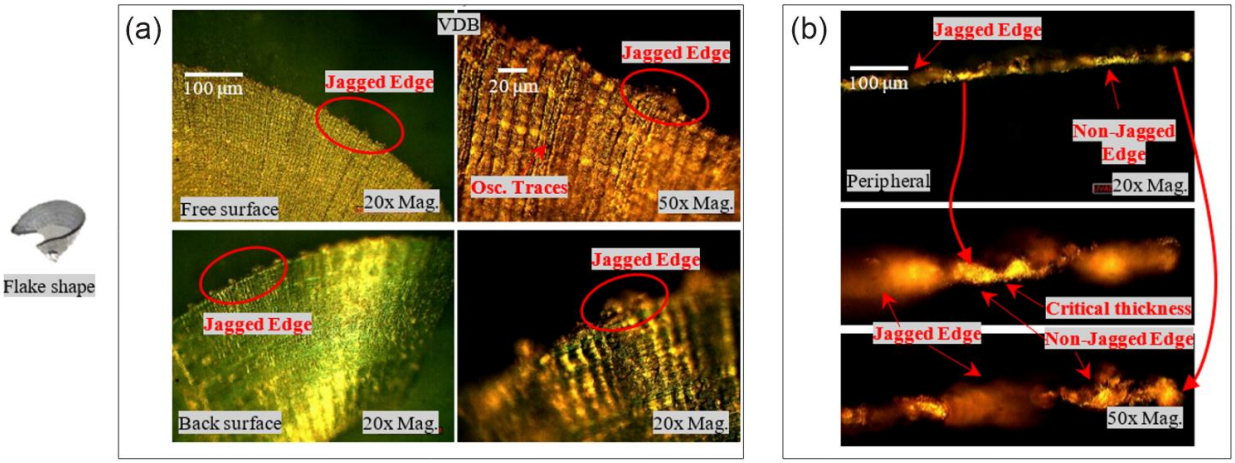


Figure 36. Flake chip topology and thickness for experiment number VDB (a) free & back surface, and (b) peripheral

Up to this point, it has been demonstrated that:

1. At an interrupted cutting trajectory, the relatively small disengagement of the tool at high frequency does not produce the discretized chip
2. The loading effect reduces the actual/effective A_o, thus lowering or preventing the disengagement of the tool during the cutting process. As result, the continuous chip may still appear, and broken chips are discretized differently with expected size as shown in kinematics
3. The oscillation traces are found in the free and back surfaces of low-feed drilling chips since the chip is relatively thin
4. The jagged edge and critical thickness promote a higher possibility of the chip break

5.2 Ultrasonic vibration-assisted drilling experiment with applicable feed per tooth

This section discussed the cutting forces and chip formation including the oscillation traces and chip shapes in CD and UVAD with applicable feed per tooth that practically used. The cutting forces are measured and compared between CD and UVAD. Furthermore, the cutting forces, oscillation traces and chip shapes are observed and correlated with the insights from kinematics and FEA.

The CNC machine, ultrasonic tool holder and dynamometer are used in this section. The drilling tool specification is shown in Table 1. The initial A_o and f_o are 16.2 µm and 25000 Hz. The peck drilling setup is used as shown in Figure 37. The drilling step is 12 mm until it reaches 24 mm drilling depth. The experiment configurations are shown in Table 5. In this configuration, only applicable feeds per tooth are considered so t_z is relatively high compared with A_o or H_w. In each experimental number, a dedicated tool is used for each cutting

parameter used to avoid the tool wear effect. Each experiment number is performed with three repetitions. In each step, the chips are collected and the cutting forces are recorded.

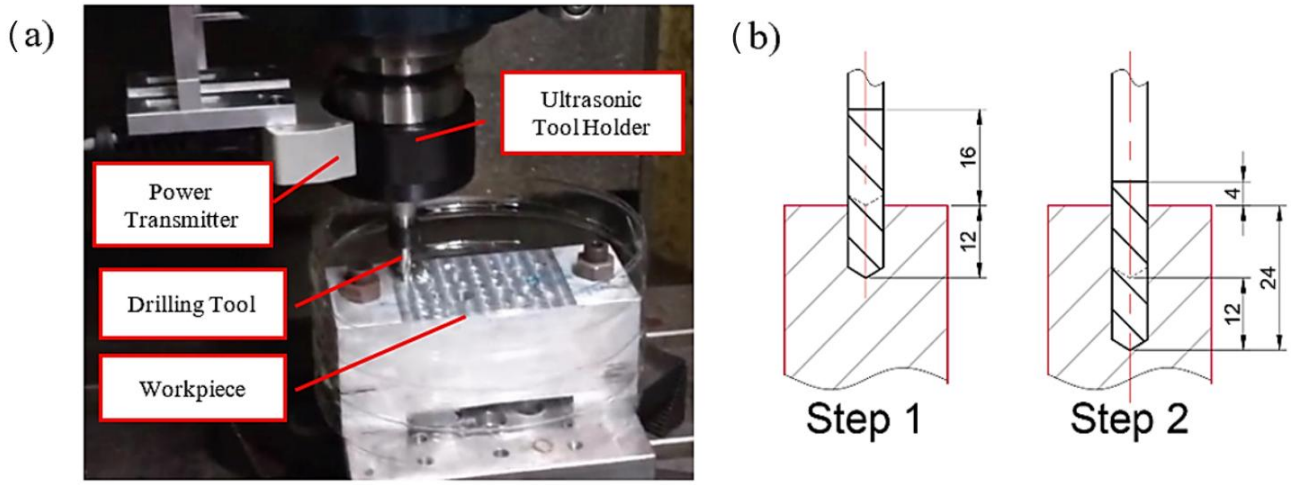


Figure 37. Experiment setup in drilling experiments; a) real condition; b) peck drilling steps

Table 5. Experiment configuration in drilling experiment with applicable parameters

Exp. No.	Drilling parameters		Oscillation parameters	
	Spindle speed (S) [rpm]	Feed per tooth (t_{z0}) [mm/tooth]	Oscillation amplitude (A_o) [µm]	Oscillation frequency (f_o) [µm]
CD0	1000	0.05	-	-
UVAD0	1000	0.05	16.2	25000
CD1A	3000	0.05	-	-
CD1B	3000	0.1		
CD2A	4000	0.05		
CD2B	4000	0.1		
VD1A	3000	0.05	16.2	25000
VD1B	3000	0.1		
VD2A	4000	0.05		
VD2B	4000	0.1		

5.2.1 Cutting forces

The cutting force which comprised as thrust force F_z and torque T_z data that is obtained from the experiment is shown in Figure 38. The F_z and T_z from each drilling step are evaluated at depth intervals as shown in Figure 37(b). Within the drilling region (DR) average and standard deviation of F_z and T_z are evaluated at depth (H) of 2-4 mm, 8-10 mm, 14-16 mm and 20-22 mm, respectively. These values are obtained from the three experimental data for each experiment number shown in Table 5.

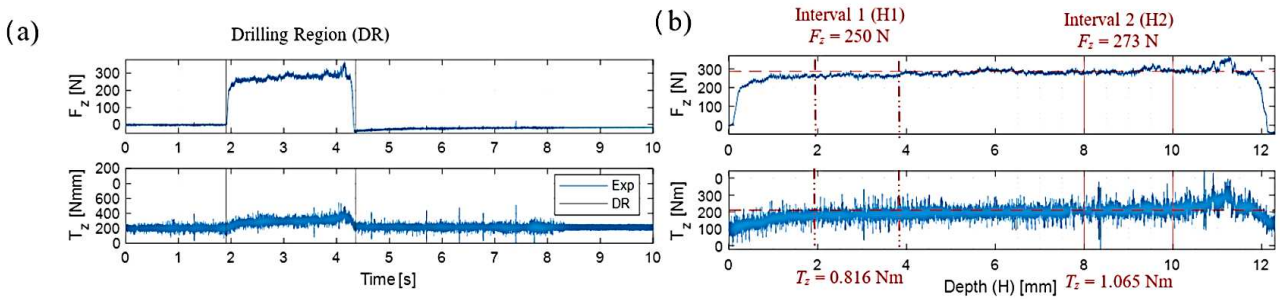


Figure 38. Thrust force and torque data for experiment VD1A at certain intervals in (a) time-domain and (b) corresponding drilling region (DR) in-depth domain

Figure 39 shows the thrust force and torque values at entry and exit depth progression for t_{z0} = 0.05 mm with two different spindle speeds (1000 and 3000 rpm). The F_z and T_z are increasing as the drilling progress is caused by the chip evacuation force. In general, it can be concluded that UVAD reduces the cutting forces. The higher spindle speeds result in better thrust forces and torque even though fluctuations occur slightly higher particularly in Tz. Moreover, several other t_{z0} values are carried out to observe the trends on the Fz and Tz at higher spindle speeds value as shown in Figure 40. Obviously, higher t_{z0} gives higher Fz and Tz. The chip evacuation in the early interval is smaller compared with the end interval. Due to higher friction at higher S and poor chip formation, overall, the average and standard deviation of F_z and T_z are increasing at deeper depth. Particularly in the current setup, it seems that the spindle speed of 3000 rpm merges as optimum spindle speed. It is expected from kinematic analysis (high λ_o) and machined surface profile point of view (adequately high L_w and H_w), the drilling process. At 4000 rpm, higher friction and poor chip formation dominate thus Fz and Tz are increasing even more with high fluctuations.

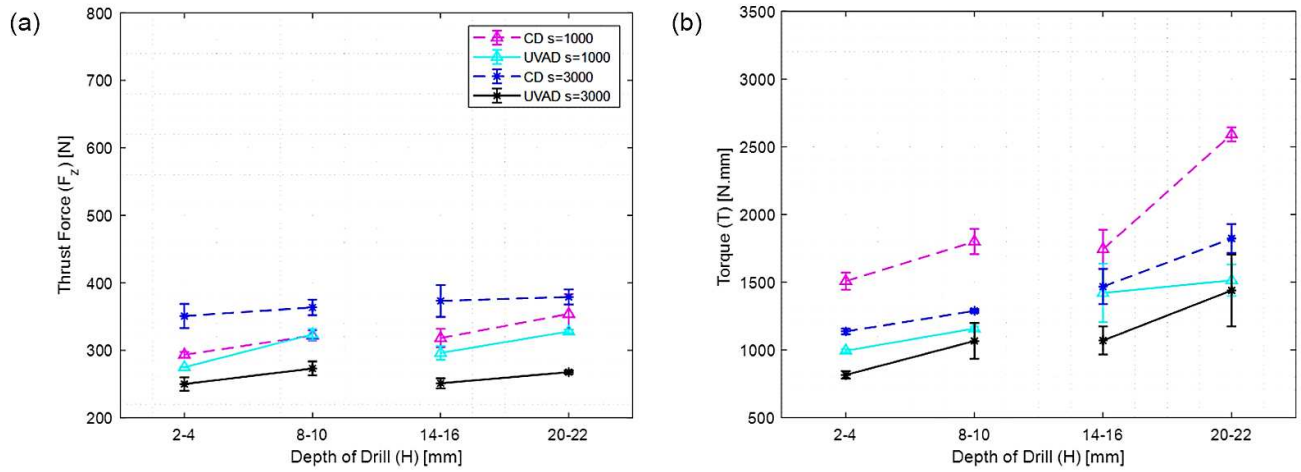


Figure 39. Force measurement for CD0 and UVAD0 (at different cutting speeds with fixed feed per tooth of 0.05 mm. (a) cutting thrust force, (b) cutting torque

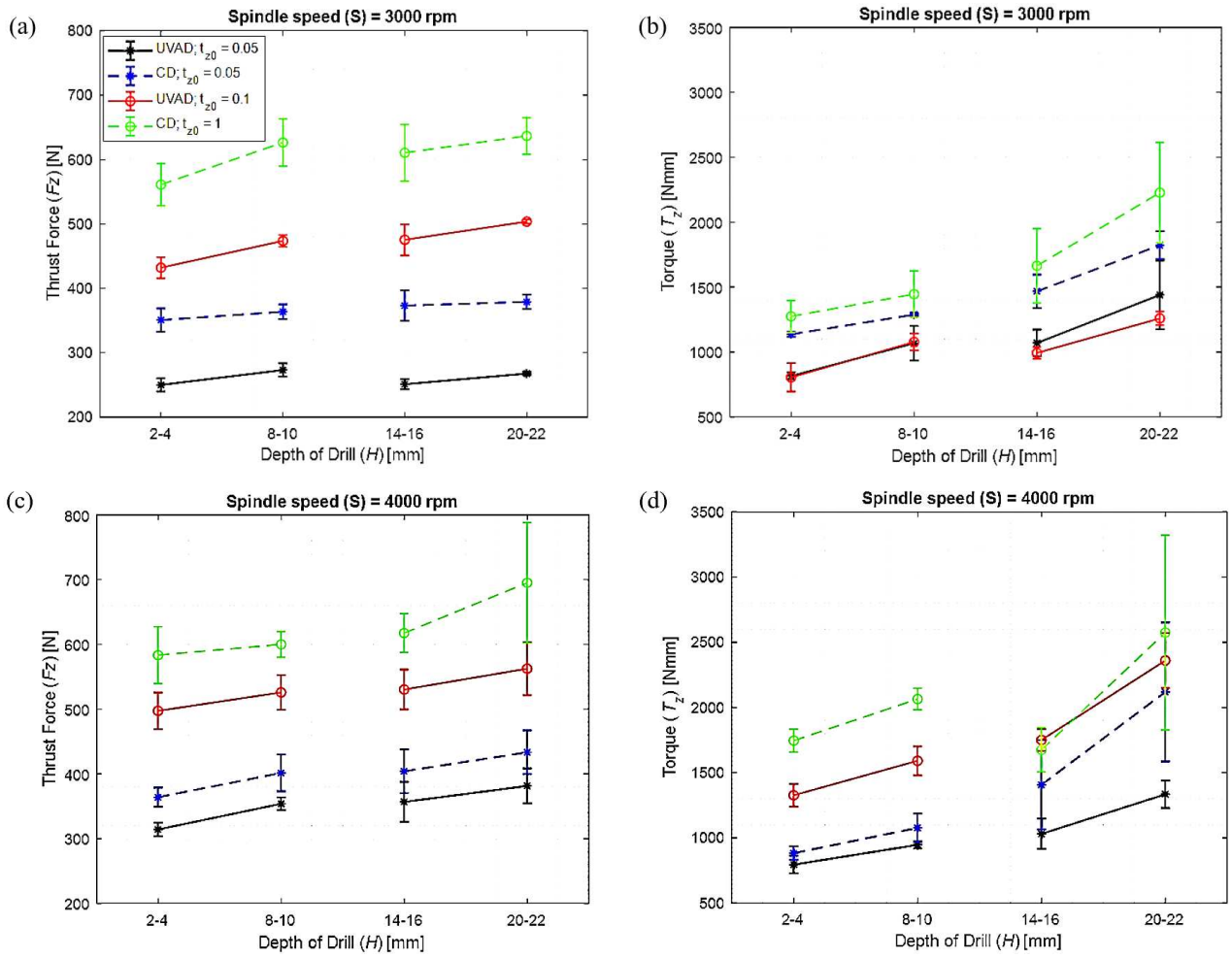


Figure 40. Thrust forces and torque for UVAD and CD with different feeds per tooth and spindle speeds. (a) cutting thrust force for 3000 rpm drilling, (b) cutting torque for 3000 rpm drilling, (c) cutting thrust force for 4000 rpm, (d) cutting torque for 4000 rpm drilling.

5.2.2 Oscillation traces and chip shapes

The dominant chip shape that is being produced during the drilling process is string chips as depicted in Figure 41. The chip is form following the peripheral direction which is also shown in Figure 13. As the chip formed, the thickness increases because the chip evacuation effect occurs. In radial direction, the chip also increases as radius increases. The back surface is one that most likely contacts with the rake face, meanwhile the free surface is one that never in contact with the tool.

Based on topology observation on the chip, no oscillation traces or compression traces are found on the back surface for both UVAD and CD as shown in Figure 42. Meanwhile, the oscillation traces are found in the free surface of the chips from UVAD. The pattern of the oscillation traces is more regular and distinct compared with the compression trace found in CD. This verifies that the machined surface profile is compressed in chip formation.

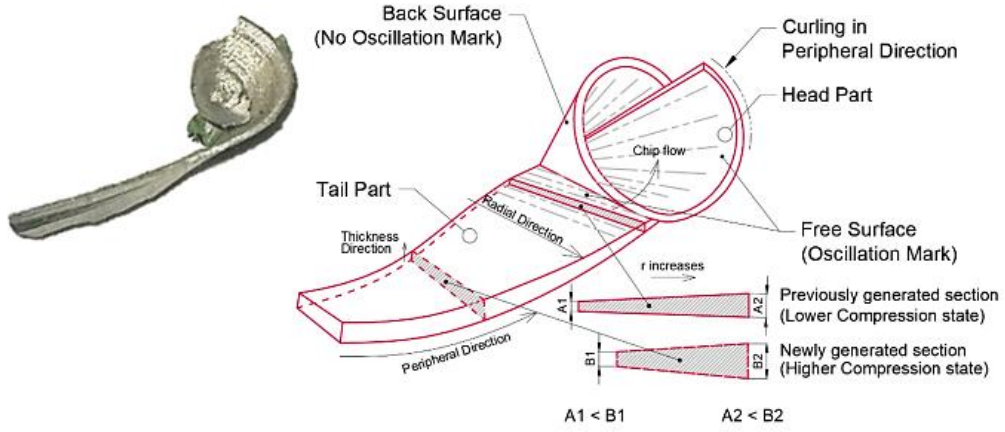


Figure 41. General string chip shape and thickness variation

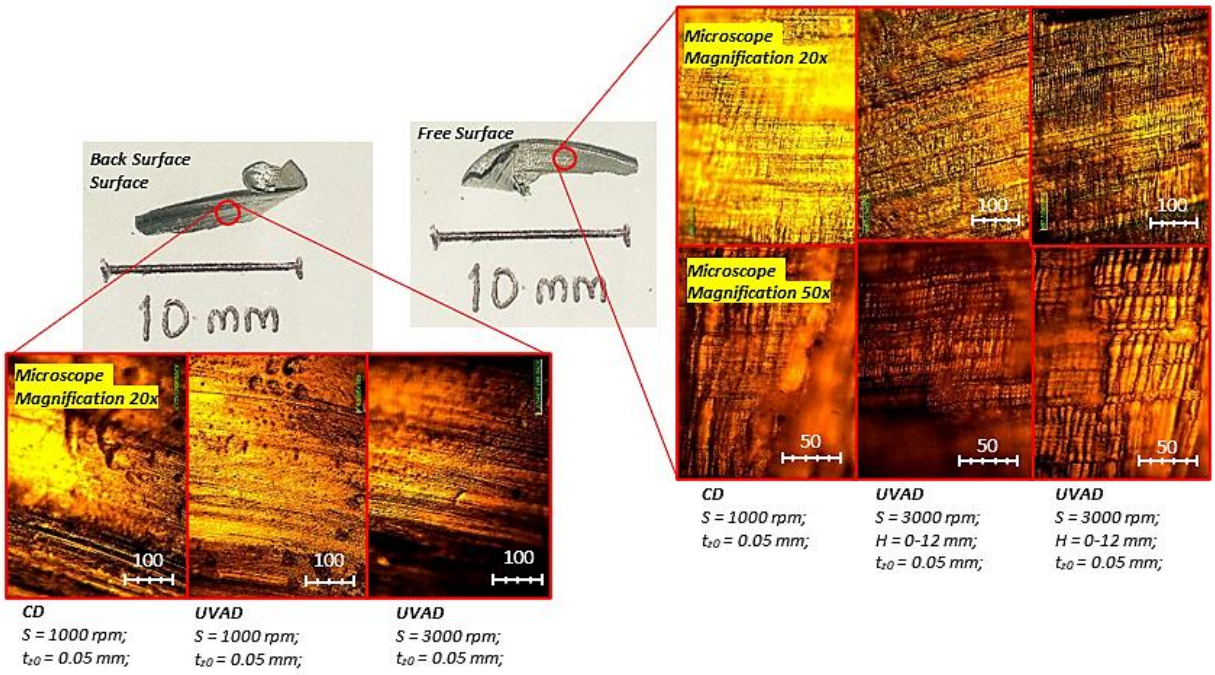


Figure 42. Oscillation marks found on the string chip in UVAD compared with CD which eventually promotes better chip breakage

Moreover, the chip thickness (t_c) of the chips is measured on the cross-section in the radial direction. Figure 43 depicts t_c measurement from the process with high t_{z0}. On average, t_c in UVAD is smaller. The observation of the compressed wavelength λ_{oc} and t_c for each experiment is presented in Table 6. It is important to note that besides the oscillation traces found in the drilling chips there is also higher curvature that occurred in the free surface due to phenomena as depicted in Figure 26 in the FEA result.

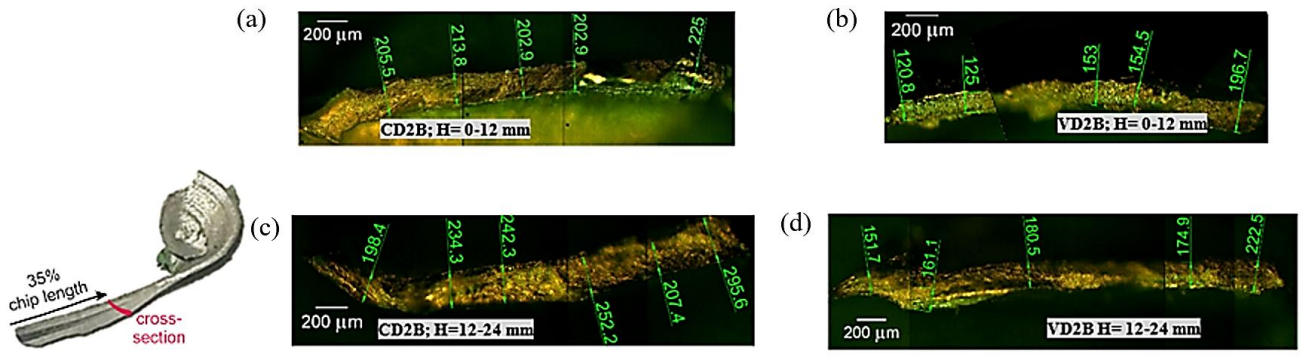


Figure 43. Chip thickness measurement in the radial direction for different depths.
(a) CD in 0-12 mm depth, (b) UVAD in 0-12mm depth, (c) CD in 12-24 mm depth,
(d) UVAD in 12-24 mm depth

The compression ratio of the wavelength (Cr_λ) is defined to represent the compression of the oscillation trace in free surface formation as found in Figure 42. It can be evaluated as:

$$Cr_\lambda = \frac{\lambda_o}{\lambda_{oc}}. \tag{23}$$

Note that based on [68], actual V_t in the string chip is uniform, so λ_o(R/2) is considered. It can be inferred that Cr_λ depends on the nominal λ_o despite different t_{z0} and H. This is inferred that the local compression zone occurred during the free surface formation. The whole material in the chip is also compressed so that Cr_{tc} is proposed. It can be evaluated as:

$$Cr_{tc} = \frac{t_{zo}}{t_c}. \tag{34}$$

Moreover, Cr_λ based on λ_o(R/2) and Cr_{tc} are approximately the same. Meanwhile, the compression ratios between on UVAD are found to be smaller compared with those in CD. This is to highlight that the chip evacuation is better facilitated in UVAD that is caused by oscillation motion on the drill grooves.

Table 6. Drilling chips observation result

Exp. No.	Depth Inter.	Wavelength [µm]				Profile Height [µm]		Chip thickness	
		Nom. λ_o(R) [µm]	Nom. λ_o(R/2) [µm]	Meas. λ_{oc} [µm]	Comp. ratio Cr_λ [ ]	Initial H_w [µm]	Meas. H_{wc} [µm]	Meas. t_c [µm]	Comp. Ratio Cr_{tc} [ ]
CD1A	H1	-	-	-	-	-	-	95.24	1.90
	H2			-	-		-	97.525	1.95
CD1B	H3			-	-		-	256.40	2.56
	H4			-	-		-	220.22	2.20
CD2A	H1	-	-	-	-	-	-	120.30	2.40
	H2			-	-		-	142.48	2.85
CD2B	H3			-	-		-	178.14	1.78
	H4			-	-		-	238.37	2.38
VD1A	H1	37.7	18.85	9.50	1.98	4.65	0.98	73.4	1.47

	H2			9.40	2.01		1.42	95.18	1.90
VD1B	H3			9.92	1.90		2.71	230.26	2.30
	H4			10.98	1.72		2.50	234.28	2.34
VD2A	H1	50.27	25.14	16.70	1.50	6.25	3.76	100.68	2.01
	H2			16.70	1.50		3.00	109.9	2.20
VD2B	H3			17.70	1.42		4.19	156	1.56
	H4			17.55	1.43		3.99	210.02	2.10

Up to this point, based on the studies and findings, it is expected that the reduction of the F_z and T_z in applicable feed per tooth is caused by several factors, including:

1. Oscillation traces that promote a higher possibility of the drilling chip break
2. Oscillation motion generates contact between the generated chip and the rake face that promotes a higher chance for the chip to break
3. Lower friction between the chips and drilling groove results in a more desirable chip shape and chip evacuation process indicated by low compression ratio

6. Conclusions and future work

This study provides an in-depth investigation into the mechanics of Ultrasonic Vibration-Assisted Drilling (UVAD) compared to Conventional Drilling (CD) through an integrated approach of kinematic modeling, finite element analysis (FEA), and experimental validation. By integrating cutting-edge twist drill geometry with kinematic modeling, it was revealed that UVAD introduces a dynamic micro-hammering effect, effective cutting speed and effective rake angle. This interaction significantly alters the machined surface topology by creating a varying effective uncut chip thickness throughout the drilling progression. Unlike the static nature of CD, the UVAD transforms the tool-workpiece engagement into a series of high-frequency intermittent contacts, fundamentally changing the material removal process.

Numerical simulations via finite element analysis demonstrated the superiority of UVAD compared with CD. The process consistently shows lower cutting forces because of the reduction in the effective contact length and time, also the alteration of the effective rake angle. These changes promote enhanced chip formation, characterized by higher curling rates, thinner chips, and weak points that facilitate a round four-time improvement in chip breakage compared to CD. Furthermore, the FEA results highlighted that UVAD produces a distinct sawtooth-like profile and induces higher compressive residual stress which affects the successive cuts

Experimental results support these findings while providing deeper insight into the influence of processing parameters and system dynamics. It was observed that UVAD significantly reduces thrust forces and torque under different drilling and oscillation parameters trials. While trajectory analysis suggested chip breakage at

the micron scale, low-feed experiments did not fully realize this effect, indicating that material elasticity or system damping may limit kinematic predictions at extreme scales. Additionally, the presence of oscillation traces and jagged edges on the chips, alongside a lower compression ratio, signifies better chip formation and breakage performance.

Finally, the study identified a critical loading effect where the physical resistance and cutting forces in the drilling influences the actual oscillation amplitudes and frequencies. This suggests that the efficiency of UVAD is not solely a function of programmed parameters but is also dependent on the stiffness of the machine-tool system. In summary, the advantages of UVAD stem from a fundamental shift in chip formation mechanics driven by the micro-hammering effect and improved friction at the tool-chip interface collectively ensuring lower energy consumption, better chip control, and superior surface integrity.

References

[1] Yadav, A. K., kumar, M., Bajpai, V., Singh, N. K., and Singh, R. K., 2017, "FE Modeling of Burr Size in High- Speed Micro-Milling of Ti6Al4V," Precis. Eng., **49**, pp. 287–292. https://doi.org/10.1016/J.PRECISIONENG.2017.02.017.

[2] Fu, Z., Zhang, X., Wang, X., and Yang, W., 2014, "Analytical Modeling of Chatter Vibration in Orthogonal Cutting Using a Predictive Force Model," Int. J. Mech. Sci., **88**, pp. 145–153. https://doi.org/10.1016/J.IJMECSCI.2014.08.005.

[3] Sokołowski, A., 2010, *On Burr Height Estimation Based on Axial Drilling Force Manufacturing and Processing*. [Online]. Available: www.journalamme.org.

[4] Hanasaki, S., Hosoi, R., Hosoi, T., and Nishimura, S., *Twist Drill Drillable Deep Hole under Continuous High Feed Rate (Mechanism of Particular Type Chip Formation of 0-Degree Rake Angle Twist Drill)*.

[5] Wang, J. J., Uhlmann, E., Oberschmidt, D., Sung, C. F., and Perfilov, I., 2016, "Critical Depth of Cut and Asymptotic Spindle Speed for Chatter in Micro Milling with Process Damping," CIRP Ann. Manuf. Technol., **65**(1), pp. 113–116. https://doi.org/10.1016/j.cirp.2016.04.088.

[6] Chandrasekharan, V., Kapoor, S. G., and DeVor, R. E., 1995, "A Mechanistic Approach to Predicting the Cutting Forces in Drilling: With Application to Fiber-Reinforced Composite Materials," J. Eng. Ind., **114**(4), pp. 559–70. https://doi.org/10.1115/1.2803534.

[7] Curnick Coleg Cymoedd, P., Charlton, P., Donne, K., Curnick, P., Kelvin Donne, P., and Thomas, R., 2011, *An Investigation into the Drilling of Carbon and Glass Fibre Reinforced Polymer Composites Virtual*

Source Aperture View Project An Investigation into the Drilling of Carbon and Glass Fibre Reinforced Polymer Composites. [Online]. Available: https://www.researchgate.net/publication/235334442.

[8] Matsumura, T., and Leopold, Jü., 2010, "Simulation of Drilling Process for Control of Burr Formation," Journal of Advanced Mechanical Design, Systems and Manufacturing, **4**(5), pp. 966–975. https://doi.org/10.1299/jamdsm.4.966.

[9] Wang, Q., Zhang, D., Chen, B., Zhang, Y., and Wu, B., 2019, "Energy Consumption Model for Drilling Processes Based on Cutting Force," Applied Sciences (Switzerland), **9**(22). https://doi.org/10.3390/app9224801.

[10] Dun, Y., Zhu, L., and Wang, S., 2019, "Investigation on Milling Force of Thin-Walled Workpiece Considering Dynamic Characteristics of Workpiece," Journal of Mechanical Science and Technology, **33**(9), pp. 4061–4079. https://doi.org/10.1007/s12206-019-0802-3.

[11] Lotfi, M., Akhavan Farid, A., and Soleimanimehr, H., 2015, "The Effect of Chip Breaker Geometry on Chip Shape, Bending Moment, and Cutting Force: FE Analysis and Experimental Study," International Journal of Advanced Manufacturing Technology, **78**(5–8), pp. 917–925. https://doi.org/10.1007/s00170-014-6676-8.

[12] Soleimanimehr, H., Nategh, M. J., Najafabadi, A. F., and Zarnani, A., 2018, "The Analysis of the Timoshenko Transverse Vibrations of Workpiece in the Ultrasonic Vibration-Assisted Turning Process and Investigation of the Machining Error Caused by This Vibration," Precis. Eng., **54**, pp. 99–106. https://doi.org/10.1016/j.precisioneng.2018.05.006.

[13] Yang, Z., Zhu, L., Zhang, G., Ni, C., and Lin, B., 2020, "Review of Ultrasonic Vibration-Assisted Machining in Advanced Materials," Int. J. Mach. Tools Manuf., **156**, p. 103594. https://doi.org/10.1016/J.IJMACHTOOLS.2020.103594.

[14] Wang, T., Liang, X., Wang, B., Liu, K., Li, T., Cai, Y., and Liu, Z., 2025, "Ultrasonic Vibration-Assisted Machining in Aerospace Composite Materials: Principle, Technology, Challenges," Compos. Part A Appl. Sci. Manuf., **199**, p. 109250. https://doi.org/10.1016/j.compositesa.2025.109250.

[15] Wang, Q., Wu, Y., Gu, J., Lu, D., Ji, Y., and Nomura, M., 2016, "Fundamental Machining Characteristics of the In-Base-Plane Ultrasonic Elliptical Vibration Assisted Turning of Inconel 718," *Procedia CIRP*, Elsevier B.V., pp. 858–862. https://doi.org/10.1016/j.procir.2016.03.008.

[16] Sharma, V., and Pandey, P. M., 2016, "Optimization of Machining and Vibration Parameters for Residual Stresses Minimization in Ultrasonic Assisted Turning of 4340 Hardened Steel," Ultrasonics, **70**, pp. 172–182. https://doi.org/10.1016/j.ultras.2016.05.001.

[17] Jamil, M. F., Li, Q., Keymanesh, M., Feng, P., and Zhang, J., 2025, "A Critical Review of Ultrasonic-Assisted Machining of Titanium Alloys," Machines, **13**(9). https://doi.org/10.3390/machines13090844.

[18] Wang, J., Shimada, K., Mizutani, M., and Kuriyagawa, T., 2018, "Effects of Abrasive Material and Particle Shape on Machining Performance in Micro Ultrasonic Machining," Precis. Eng., **51**, pp. 373–387. https://doi.org/10.1016/J.PRECISIONENG.2017.09.008.

[19] Gu, G., Wu, S., Wang, D., Zhou, S., Zhu, L., An, Q., Guo, H., and Li, C., 2023, "A Review of the Research on the Variation of Tool's Motion Trajectory and Its Influence on the Formation Mechanism of Surface Quality in Ultrasonic Vibration Machining," J. Manuf. Process., **107**, pp. 294–319. https://doi.org/10.1016/j.jmapro.2023.10.025.

[20] Zheng, L., Chen, W., and Huo, D., 2020, "Review of Vibration Devices for Vibration-Assisted Machining," The International Journal of Advanced Manufacturing Technology, **108**(5–6), pp. 1631–1651. https://doi.org/10.1007/s00170-020-05483-8.

[21] Brehl, D. E., and Dow, T. A., 2008, "Review of Vibration-Assisted Machining," Precis. Eng., **32**(3), pp. 153–172. https://doi.org/10.1016/j.precisioneng.2007.08.003.

[22] Flórez García, L. C., González Rojas, H. A., and Sánchez Egea, A. J., 2020, "Estimation of Specific Cutting Energy in an S235 Alloy for Multi-Directional Ultrasonic Vibration-Assisted Machining Using the Finite Element Method," Materials 2020, Vol. 13, Page 567, **13**(3), p. 567. https://doi.org/10.3390/MA13030567.

[23] El-Asfoury, M. S., Baraya, M., El Shrief, E., Abdelgawad, K., Sultan, M., and Abass, A., 2024, "AI-Based Prediction of Ultrasonic Vibration-Assisted Milling Performance," Sensors, **24**(17). https://doi.org/10.3390/s24175509.

[24] Khan, M. A., Ali, A. B. M., Ullah, S., Khaqan, A. M., Khan, M. I., Umeed, M., and Ben Khedher, N., 2025, "Review on the Application of Ultrasonic Vibration-Assisted Turning in Enhancing Machinability of Ti-6Al-4V Alloy," Results in Materials, **28**. https://doi.org/10.1016/j.rinma.2025.100792.

[25] Zhou, T., Niu, Y., Sun, Z., Niu, J., and Jiao, F., 2026, "Surface and Subsurface Damage Suppression in Ultrasonic Vibration Assisted Machining of Hard and Brittle Materials: A Review," Mater. Sci. Semicond. Process., **209**, p. 110628. https://doi.org/10.1016/j.mssp.2026.110628.

[26] Ni, C., Zhu, L., and Yang, Z., 2019, "Comparative Investigation of Tool Wear Mechanism and Corresponding Machined Surface Characterization in Feed-Direction Ultrasonic Vibration Assisted Milling of Ti–6Al–4V from Dynamic View," Wear, **436–437**. https://doi.org/10.1016/j.wear.2019.203006.

[27] Xiong, Y. feng, Liu, C., Wang, W. hu, Jiang, R. song, Huang, B., Wang, D. hui, and Zhang, S. guo, 2023, "Assessment of Machined Surface for SiCf/SiC Ceramic Matrix Composite during Ultrasonic Vibration-Assisted Milling-Grinding," Ceram. Int., **49**(3), pp. 5345–5356. https://doi.org/10.1016/j.ceramint.2022.10.058.

[28] Ali, S. H., Zhang, M., Liu, G., Zhao, B., Ding, W., Jamil, M., Mohan, M., Waris, H., Khan, A., and Hussain, S., 2025, "Advancing the Machinability and Tribological Characteristics of AISI 9310 Steel Using a Novel Ultrasonic Vibration-Assisted MQL Approach," J. Manuf. Process., **145**, pp. 99–115. https://doi.org/10.1016/j.jmapro.2025.04.022.

[29] Wang, J., Shimada, K., Mizutani, M., and Kuriyagawa, T., 2018, "Tool Wear Mechanism and Its Relation to Material Removal in Ultrasonic Machining," Wear, **394–395**, pp. 96–108. https://doi.org/10.1016/J.WEAR.2017.10.010.

[30] Chen, W., Teng, X., Zheng, L., Xie, W., and Huo, D., 2018, "Burr Reduction Mechanism in Vibration-Assisted Micro Milling," Manuf. Lett., **16**, pp. 6–9. https://doi.org/10.1016/J.MFGLET.2018.02.015.

[31] Lu, H., Zhu, L., Wang, S., Yan, B., Xue, P., Hao, Y., Ning, J., Xu, P., and Qin, S., 2023, "The Machinability and Anisotropy of Bio-CoCrMo Manufactured by Directed Energy Deposition in Ultrasonic Vibration Assisted Drilling," Journal of Materials Research and Technology, **26**, pp. 1238–1259. https://doi.org/10.1016/j.jmrt.2023.07.251.

[32] Gao, H., Ma, B., Zhu, Y., and Yang, H., 2022, "Enhancement of Machinability and Surface Quality of Ti-6Al-4V by Longitudinal Ultrasonic Vibration-Assisted Milling under Dry Conditions," Measurement (Lond)., **187**. https://doi.org/10.1016/j.measurement.2021.110324.

[33] Liu, Y., Li, C., Hu, Y., Zakharov, O., Cui, H., Wu, M., Yan, Y., and Geng, Y., 2024, "Damage and Removal Behaviors of Indium Phosphide Crystals Involved in Ultrasonic Vibration-Assisted AFM Machining," Mater. Today Commun., **41**. https://doi.org/10.1016/j.mtcomm.2024.110792.

[34] Zhu, Z., Guo, K., Sun, J., Li, J., Liu, Y., Zheng, Y., and Chen, L., 2018, "Evaluation of Novel Tool Geometries in Dry Drilling Aluminium 2024-T351/Titanium Ti6Al4V Stack," J. Mater. Process. Technol., **259**, pp. 270–281. https://doi.org/10.1016/j.jmatprotec.2018.04.044.

[35] Zhang, J., Luo, D., Gao, W., Luo, T., Deng, C., Tao, G., and Cao, H., 2026, "Machining Mechanism in 2D Large-Amplitude Ultrasonic Vibration Assisted Milling of CF/PEEK Composites," Chinese Journal of Mechanical Engineering, **39**, p. 100114. https://doi.org/10.1016/j.cjme.2025.100114.

[36] Namlu, R. H., Lotfi, B., and Kılıç, S. E., 2024, "Enhancing Machining Efficiency of Ti-6Al-4V through Multi-Axial Ultrasonic Vibration-Assisted Machining and Hybrid Nanofluid Minimum Quantity Lubrication," J. Manuf. Process., **119**, pp. 348–371. https://doi.org/10.1016/j.jmapro.2024.03.073.

[37] Blasl, J., Lichtinger, K., Vieltorf, F., Zaeh, M. F., and Hanenkamp, N., 2024, "Experimental Investigation of Ultrasonic Vibration-Assisted Cryogenic Minimum Quantity Lubrication for Milling of Ti-6Al-4V and Grinding of Zerodur," Production Engineering, **18**(1), pp. 75–86. https://doi.org/10.1007/s11740-023-01214-6.

[38] Chaudhari, A., Sharma, A., Awale, A. S., Yusufzai, M. Z. K., and Vashista, M., 2022, "Modeling and Simulation Study of Dry Ultrasonic Vibration-Assisted Grinding of Tool Steel With Single Alumina Abrasive Grit," J. Manuf. Sci. Eng., **144**(11). https://doi.org/10.1115/1.4054602.

[39] Hao, Z., Zhang, H., and Fan, Y., 2025, "Tool Wear Mathematical Model of PCD during Ultrasonic Elliptic Vibration Cutting SiCp/Al Composite," Int. J. Refract. Metals Hard Mater., **126**, p. 106967. https://doi.org/10.1016/j.ijrmhm.2024.106967.

[40] Ni, C., and Zhu, L., 2020, "Investigation on Machining Characteristics of TC4 Alloy by Simultaneous Application of Ultrasonic Vibration Assisted Milling (UVAM) and Economical-Environmental MQL Technology," J. Mater. Process. Technol., **278**. https://doi.org/10.1016/j.jmatprotec.2019.116518.

[41] Zhao, S., Zhang, H., Peng, F., Tang, X., Sun, H., and Yan, R., 2024, "United Optimization Strategy of Ultrasonic Vibration Assisted Process and Multiple Parameters for Machining Deformation Reduction," J. Manuf. Process., **131**, pp. 1942–1958. https://doi.org/10.1016/j.jmapro.2024.09.111.

[42] Xu, P., Yin, J., Liu, G., Su, H., Ding, W., and Xu, J., 2024, "Machinability of Submillimeter Holes in Ceramic Matrix Composites by High-Frequency Ultrasonic Vibration-Assisted Drilling," J. Mater. Process. Technol., **328**. https://doi.org/10.1016/j.jmatprotec.2024.118409.

[43] Gao, S., Wang, X., Zhao, D., Zheng, M., Xin, T., and Gu, Y., 2026, "Ultrasonically Assisted Milling of Internal Threads in an NC19FeNb Superalloy: Tool Wear Mechanisms and Machining Performance," Wear, p. 206823. https://doi.org/10.1016/j.wear.2026.206823.

[44] Liu, W., Shan, C., Wang, S., Jia, F., and Xia, Z., 2026, "Ultrasonic Vibration Assisted Milling of C/C Composites: Mechanism, Machining Characteristics, and Parameters Optimization," Compos. B Eng., **316**, p. 113555. https://doi.org/10.1016/j.compositesb.2026.113555.

[45] Ni, C., Zhu, L., Liu, C., and Yang, Z., 2018, "Analytical Modeling of Tool-Workpiece Contact Rate and Experimental Study in Ultrasonic Vibration-Assisted Milling of Ti–6Al–4V," Int. J. Mech. Sci., **142–143**, pp. 97–111. https://doi.org/10.1016/j.ijmecsci.2018.04.037.

[46] Verma, G. C., Pandey, P. M., and Dixit, U. S., 2018, "Modeling of Static Machining Force in Axial Ultrasonic-Vibration Assisted Milling Considering Acoustic Softening," Int. J. Mech. Sci., **136**, pp. 1–16. https://doi.org/10.1016/j.ijmecsci.2017.11.048.

[47] Xie, Z., Liu, Z., Han, L., Wang, B., Xin, M., Cai, Y., and Song, Q., 2022, "Optimizing Amplitude to Improve Machined Surface Quality in Longitudinal Ultrasonic Vibration-Assisted Side Milling 2.5D C/SiC Composites," Compos. Struct., **297**. https://doi.org/10.1016/j.compstruct.2022.115963.

[48] Chen, X., Shao, W., Tang, J., Zhou, Y., Kontziampasis, D., Mo, S., and Hu, B., 2025, "Study on the Transient Thermo-Mechanical Coupling Mechanism at Tool-Chip Interface in Ultrasonic Vibration Assisted Chip Formation Process under Sustainable Dry Machining Conditions," Clean. Eng. Technol., **25**. https://doi.org/10.1016/j.clet.2025.100908.

[49] Yin, H., Xie, Z., Zhou, Q., Xiang, J., Lai, K. hung, Wiercigroch, M., and Cai, W., 2025, "Mechanism of a Novel Parallel Ultrasonic Vibration-Assisted Cutting System for High Performance Machining," Mech. Syst. Signal Process., **238**. https://doi.org/10.1016/j.ymssp.2025.113213.

[50] Yin, H., Xie, Z., Zhou, Q., Xiang, J., Lai, K., Wiercigroch, M., and Cai, W., 2025, "Mechanism of a Novel Parallel Ultrasonic Vibration-Assisted Cutting System for High Performance Machining," Mech. Syst. Signal Process., **238**, p. 113213. https://doi.org/10.1016/j.ymssp.2025.113213.

[51] Song, C., Xiang, D., Li, Y., Zhang, Z., Yang, S., Gao, G., and Cui, X., 2025, "Multi-Dimensional Ultrasonic Assisted Microscale Scratching of Fe-Cr Alloys," Int. J. Mech. Sci., **305**. https://doi.org/10.1016/j.ijmecsci.2025.110806.

[52] Teng, H., Chen, S., Kurniawan, R., Li, S., Li, C., Xu, M., Chen, J., and Ko, T. J., 2025, "Brittle–Ductile Transition Model for Ultrasonic Vibration–Assisted Blade Dicing," Int. J. Mech. Sci., **293**. https://doi.org/10.1016/j.ijmecsci.2025.110196.

[53] Sun, L., Zhang, S., Chen, M., Yin, T., To, S., Wu, Y., and Yip, W. S., 2025, "Ultrasonic-Assisted Ultra-Precision Turning of Zinc-Selenide with Straight-Nosed Diamond Tools," Int. J. Mech. Sci., **285**. https://doi.org/10.1016/j.ijmecsci.2024.109823.

[54] Zhang, Y., Soo, S. L., and Hood, R., 2025, "Semi-Analytical Modelling of Forces and Tool Wear in Ultrasonic-Assisted Milling," Int. J. Mech. Sci., **304**. https://doi.org/10.1016/j.ijmecsci.2025.110718.

[55] Lo, S.-P., 2000, "An Analysis of Cutting under Different Rake Angles Using the Finite Element Method," J. Mater. Process. Technol., **105**(1–2), pp. 143–151. https://doi.org/10.1016/S0924-0136(00)00650-6.

[56] Reddy, L. V. K., Prasad, B. S., and Rajasekhar, M., 2021, "Analysis of Vibration Assisted Dry End Milling Using 3D FE Simulation – An Investigational Approach," Mater. Today Proc., **45**, pp. 3075–3084. https://doi.org/10.1016/J.MATPR.2020.12.063.

[57] Lotfi, M., Amini, S., and Aghaei, M., 2018, "3D FEM Simulation of Tool Wear in Ultrasonic Assisted Rotary Turning," Ultrasonics, **88**, pp. 106–114. https://doi.org/10.1016/J.ULTRAS.2018.03.013.

[58] Cui, F., Zhang, H., Yang, M., Deng, B., Tang, X., Peng, F., Yan, R., and Pan, Z., 2025, "Multiscale Simulation and Experimental Study on Ultrasonic Vibration Assisted Machining of SiCp/Al Composites Considering Acoustic Softening," J. Mater. Process. Technol., **335**. https://doi.org/10.1016/j.jmatprotec.2024.118649.

[59] Hu, W., Du, P., Qiu, X., Zhao, X., Hu, Z., Zhang, J., and Liu, Y., 2022, "Enhanced Dry Machinability of TC4 Titanium Alloy by Longitudinal-Bending Hybrid Ultrasonic Vibration-Assisted Milling," J. Clean. Prod., **379**. https://doi.org/10.1016/j.jclepro.2022.134866.

[60] Kim, J., Zani, L., Abdul-Kadir, A., Roy, A., Baxevanakis, K. P., Jones, L. C. R., and Silberschmidt, V. V., 2023, "Hybrid-Hybrid Turning of Micro-SiCp/AA2124 Composites: A Comparative Study of Laser-and-Ultrasonic Vibration-Assisted Machining," J. Manuf. Process., **86**, pp. 109–125. https://doi.org/10.1016/j.jmapro.2022.12.045.

[61] Gao, G., Wang, H., Li, R., Zhang, B., Ma, W., Xiang, D., and Ma, J., 2025, "Modeling of Axial Force and Torque in UAD of Polycrystalline 3C-SiC," Int. J. Mech. Sci., **302**. https://doi.org/10.1016/j.ijmecsci.2025.110559.

[62] Shaw, M. C.., 2005, *Metal Cutting Principles*, Oxford University Press.

[63] Armarego, E. J. A., and Cheng~, C. Y., 1972, "DRILLING WITH FLAT RAKE FACE AND CONVENTIONAL TWIST DRILLS-I. THEORETICAL INVESTIGATION," Int. J. Mach. Tool Des. Res, **12**, pp. 17–35. https://doi.org/10.1016/0020-7357(72)90009-1.

[64] Wang, Q., Jia, X., Hu, B., and Xia, W., 2019, "A Mechanistic Prediction Model of Instantaneous Cutting Forces in Drilling of Carbon Fiber-Reinforced Polymer," International Journal of Advanced Manufacturing Technology, **103**(5–8), pp. 1977–1988. https://doi.org/10.1007/s00170-019-03571-y.

[65] Aksu, B., Çelebi, C., and Budak, E., 2016, "An Experimental Investigation of Oblique Cutting Mechanics," Machining Science and Technology, **20**(3), pp. 495–521. https://doi.org/10.1080/10910344.2016.1196458.

[66] Stephenson~, D. A., 1992, "CALCULATION OF MAIN CUTTING EDGE FORCES AND TORQUE FOR DRILLS WITH ARBITRARY POINT GEOMETRIES," Int. J. Mach. Tools Manufact, **32**(4), pp. 521–538. https://doi.org/10.1016/0890-6955(92)90043-G.

[67] Mellinger, J. C., Ozdoganlar, O. B., DeVor, R. E., and Kapoor, S. G., 2002, "Modeling Chip-Evacuation Forces and Prediction of Chip-Clogging in Drilling," J. Manuf. Sci. Eng., **124**(3), pp. 605–614. https://doi.org/10.1115/1.1473146.

[68] Ke, F., Ni, J., and Stephenson, D. A., 2006, "Chip Thickening in Deep-Hole Drilling," Int. J. Mach. Tools Manuf., **46**(12–13), pp. 1500–1507. https://doi.org/10.1016/j.ijmachtools.2005.09.022.

[69] Chang, S. S. F., and Bone, G. M., 2009, "Thrust Force Model for Vibration-Assisted Drilling of Aluminum 6061-T6," Int. J. Mach. Tools Manuf., **49**(14), pp. 1070–1076. https://doi.org/10.1016/j.ijmachtools.2009.07.011.

[70] Yang, H., Ding, W., Chen, Y., Laporte, S., Xu, J., and Fu, Y., 2019, "Drilling Force Model for Forced Low Frequency Vibration Assisted Drilling of Ti-6Al-4V Titanium Alloy," Int. J. Mach. Tools Manuf., **146**. https://doi.org/10.1016/j.ijmachtools.2019.103438.

[71] Le Dref, J., Landon, Y., Dessein, G., Espinosa, C., and Dref, L., 2016, "Modelling Kinematics and Cutting Forces in Vibration Assisted Drilling," AFM, **17**(3), pp. 1–10. https://doi.org/10.1051/meca/2015078ï.

[72] Chen, S., Zou, P., Wu, H., Kang, D., and Wang, W., 2019, "Mechanism of Chip Formation in Ultrasonic Vibration Drilling and Experimental Research," Proc. Inst. Mech. Eng. C J. Mech. Eng. Sci., **233**(15), pp. 5214–5226. https://doi.org/10.1177/0954406219848464.

[73] Chen, S., Zou, P., Tian, Y., Duan, J., and Wang, W., 2019, "Study on Modal Analysis and Chip Breaking Mechanism of Inconel 718 by Ultrasonic Vibration-Assisted Drilling," International Journal of Advanced Manufacturing Technology, **105**(1–4), pp. 177–191. https://doi.org/10.1007/s00170-019-04155-6.

[74] Duman, E., Yapan, Y. F., and Uysal, A., 2025, "Synergistic Effects of Ultrasonic Vibration and Nanofluid-MQL on Surface Integrity in Sustainable Machining of Ti-6Al-7Nb Alloy," CIRP J. Manuf. Sci. Technol., **63**, pp. 281–298. https://doi.org/10.1016/j.cirpj.2025.09.017.

[75] Georgi, O., Rüger, C., Rentzsch, H., and Putz, M., "Kinematic Analysis and Process Stability of Ultrasonic-Assisted Drilling." https://doi.org/10.1007/s00170-021-07165-5/Published.

[76] Zhang, K., Wu, X., Lin, S., Zhang, Y., Shen, J., and Huang, F., 2026, "Predictive Model for Cutting Forces in Ultrasonic-Assisted Friction Drilling of Ti-6Al-4V," Int. J. Mech. Sci., **314**. https://doi.org/10.1016/j.ijmecsci.2026.111385.

[77] Zhang, C., Li, H., Zhang, X., An, Q., and Chen, M., 2025, "Parameter Optimization, Machining Quality, Removal Mechanism, and Tool Wear in Ultrasonic-Vibration-Assisted Micro-Hole Drilling Process of Cf/SiC Ceramic Matrix Composites," Ceram. Int., **51**(29), pp. 60645–60656. https://doi.org/10.1016/j.ceramint.2025.10.260.

[78] Chen, D., Zheng, Z., Ding, J., Zhang, J., Chen, X., Xiao, J., and Xu, J., 2025, "Investigation on Machining Mechanism and Surface Integrity of Sip/Al Composites with Ultrasonic Vibration-Assisted Epoxy Coating Cutting," J. Manuf. Process., **146**, pp. 427–444. https://doi.org/10.1016/j.jmapro.2025.05.009.

[79] Öztürk, E., 2026, "Analysis of Machining Performance in Ultrasonic-Assisted Drilling of Al6061 Using a Micro-Textured Drill Bit: A Validated Finite Element Method," J. Manuf. Process., **170**, pp. 118–126. https://doi.org/10.1016/j.jmapro.2026.05.013.

[80] Xu, M., Yang, Y., Chu, X., Cao, L., Li, J., Ge, J., Chen, S., Adzah, D., Ali, S., Cai, W., Li, C., and Ko, T. J., 2026, "Comprehensive Study of Machining Mechanism, Experimental Measurement and Numerical Analysis in Ultrasonic-Assisted Micro-Drilling of Printed Circuit Board," Measurement, **271**, p. 120954. https://doi.org/10.1016/j.measurement.2026.120954.

[81] Stephenson, D. A., and Agapiou, J. S., 1992, "CALCULATION OF MAIN CUTTING EDGE FORCES AND TORQUE FOR DRILLS WITH ARBITRARY POINT GEOMETRIES," Int. J. Mach. Tools Manufact, **32**(4), pp. 521–538. https://doi.org/10.1016/0890-6955(92)90043-G.

[82] Stephenson, D. A., and SMWu Research Professor Fellow, L., 1988, "Computer Models for the Mechanics of Three-Dimensional Cutting Processes-Part II: Results for Oblique End Turning and Drilling," J. Eng. Ind., **110**, pp. 32–7. https://doi.org/10.1115/1.3187839.

[83] Han, C., Zhang, D., Luo, M., and Wu, B., 2018, "Chip Evacuation Force Modelling for Deep Hole Drilling with Twist Drills," International Journal of Advanced Manufacturing Technology, **98**(9–12), pp. 3091–3103. https://doi.org/10.1007/s00170-018-2488-6.

[84] Sambhav, K., Tandon, P., and Dhande, S. G., 2012, "Geometric Modeling and Validation of Twist Drills with a Generic Point Profile," Appl. Math. Model., **36**(6), pp. 2384–2403. https://doi.org/10.1016/j.apm.2011.08.034.

[85] Armarego, E. J. A., and Cheng~, C. Y., 1972, "DRILLING WITH FLAT RAKE FACE AND CONVENTIONAL TWIST DRILLS-I. THEORETICAL INVESTIGATION," Int. J. Mach. Tool Des. Res, **12**, pp. 17–35. https://doi.org/10.1016/0020-7357(72)90009-1.

[86] Chandrasekharan, V., Kapoor, S. G., and DeVor, R. E., 1995, "A Mechanistic Approach to Predicting the Cutting Forces in Drilling: With Application to Fiber-Reinforced Composite Materials," J. Eng. Ind., **117**(4), pp. 559–0. https://doi.org/10.1115/1.2803534.

[87] Merchant, M. E., 1945, "Mechanics of the Metal Cutting Process. I. Orthogonal Cutting and a Type 2 Chip," J. Appl. Phys., **16**(5), pp. 267–275. https://doi.org/10.1063/1.1707586.

[88] Stabler, G. V., 1951, "The Fundamental Geometry of Cutting Tools," Proceedings of the Institution of Mechanical Engineers, **165**(1), pp. 14–26. https://doi.org/10.1243/pime_proc_1951_165_008_02.

[89] Jerez-Mesa, R., 2024, "Microtexturing of Industrial Surfaces via Radial Ultrasonic Vibration-Assisted Machining: An Analytical Model and Experimental Validation," Surf. Coat. Technol., **482**. https://doi.org/10.1016/j.surfcoat.2024.130718.

[90] Sajjady, S. A., Nouri Hossein Abadi, H., Amini, S., and Nosouhi, R., 2016, "Analytical and Experimental Study of Topography of Surface Texture in Ultrasonic Vibration Assisted Turning," Mater. Des., **93**, pp. 311–323. https://doi.org/10.1016/J.MATDES.2015.12.119.

[91] Onikura, H., and Ohnishi, O., 1998, "Drilling Mechanisms in Ultrasonic-Vibration Assisted Microdrilling," Journal of The Japan Society for Precision Engineering, **64**, pp. 1633–1637. https://doi.org/10.2493/JJSPE.64.1633.

[92] Ke, F., Ni, J., and Stephenson, D. A., 2005, "Continuous Chip Formation in Drilling," Int. J. Mach. Tools Manuf., **45**(15), pp. 1652–1658. https://doi.org/10.1016/j.ijmachtools.2005.03.011.

[93] Chen, X., Shao, W., Tang, J., Zhou, Y., Kontziampasis, D., Mo, S., and Hu, B., 2025, "Study on the Transient Thermo-Mechanical Coupling Mechanism at Tool-Chip Interface in Ultrasonic Vibration Assisted Chip Formation Process under Sustainable Dry Machining Conditions," Clean. Eng. Technol., **25**, p. 100908. https://doi.org/10.1016/j.clet.2025.100908.

[94] 2009, "Finite Element Modeling to Verify Residual Stress in Orthogonal Machining."

[95] Spear, D. G., Palazotto, A. N., and Kemnitz, R. A., 2021, "Modeling and Simulation Techniques Used in High Strain Rate Projectile Impact," Mathematics, **9**(3), pp. 1–29. https://doi.org/10.3390/math9030274.

[96] Berghuvud, A., Eng, M., Melender, A., Kimab, S., Stenberg, N., Thoors, H., Sc, M., and Prasad, C. S., 2009, *Finite Element Modeling to Verify Residual Stress in Orthogonal Machining*.

[97] Kao, C. C., and Wang, J. J., 2021, "Drilling Force Model Considering the Effect of Chip-Evacuation Forces," Master Thesis, National Cheng Kung University .

[98] Yin, S., Yip, W. S., Dong, Z., Kang, R., and To, S., 2025, "Experimental and Simulation Investigation of Ultrasonic Elliptical Vibration Cutting of Tungsten Alloys in Ultra-Precision Machining," Journal of Materials Research and Technology, **34**, pp. 77–89. https://doi.org/10.1016/j.jmrt.2024.12.026.

[99] Cui, F., Zhang, H., Yang, M., Deng, B., Tang, X., Peng, F., Yan, R., and Pan, Z., 2025, "Multiscale Simulation and Experimental Study on Ultrasonic Vibration Assisted Machining of SiCp/Al Composites Considering Acoustic Softening," J. Mater. Process. Technol., **335**, p. 118649. https://doi.org/10.1016/j.jmatprotec.2024.118649.

[100] Wang, L., Gao, X., Feng, Q., Guo, X., Li, Z., An, W., Xu, W., Li, Q., and Yuan, S., 2025, "How Does Ultrasonic Cutting Affect the Macroscopic Deformation and Microstructure Evolution of Fibre-Reinforced Titanium Matrix Composites?," Int. J. Mach. Tools Manuf., **205**, p. 104245. https://doi.org/10.1016/j.ijmachtools.2024.104245.

[101] Bakhshan, H., Oñate, E., and Carbonell, J. M., 2025, "A Microstructure-Integrated Acoustoplastic Constitutive Model for Ultrasonic-Assisted Machining of Ti6Al4V Alloy," CIRP J. Manuf. Sci. Technol., **57**, pp. 14–31. https://doi.org/10.1016/j.cirpj.2024.12.007.

[102] Rauf, A., Khan, M. A., Jaffery, S. H. I., and Butt, S. I., 2024, "Effects of Machining Parameters, Ultrasonic Vibrations and Cooling Conditions on Cutting Forces and Tool Wear in Meso Scale Ultrasonic Vibrations Assisted End-Milling (UVAEM) of Ti–6Al–4V under Dry, Flooded, MQL and Cryogenic Environments – A Statistical Analysis," Journal of Materials Research and Technology, **30**, pp. 8287–8303. https://doi.org/10.1016/j.jmrt.2024.05.202.

[103] Cui, F., Luo, M., Yang, M., Deng, B., Yan, R., Peng, F., Zhang, H., and Pan, Z., 2025, "Towards Understanding the Surface/Subsurface Formation Mechanism of Ultrasonic Vibration Assisted Machining of SiCp/Al Composites under Different Amplitudes," Precis. Eng., **95**, pp. 526–537. https://doi.org/10.1016/j.precisioneng.2025.05.021.

[104] Cui, F., Luo, M., Yang, M., Deng, B., Yan, R., Peng, F., Zhang, H., and Pan, Z., 2025, "Towards Understanding the Surface/Subsurface Formation Mechanism of Ultrasonic Vibration Assisted Machining of SiCp/Al Composites under Different Amplitudes," Precis. Eng., **95**, pp. 526–537. https://doi.org/10.1016/j.precisioneng.2025.05.021.

Statements & Declarations

Funding

The authors thank the King Fahd University of Petroleum and Minerals and Interdisciplinary Research Center for Intelligent Manufacturing and Robotics for providing financial aid and technical support.

Competing Interests

The authors have no relevant financial or non-financial interests to disclose

Availability of Data and Materials

The data generated during and/or analyzed during the current study are available from the corresponding author on reasonable request.

Appendix A

Figure A.1 shows the details of cutting point positions along with the coordinate system used and drill dimensions involved that eventually lead to determination of the rake angle and flank angle at certain radius. Figure A.1 (a) shows the 3D view of the polar coordinate system, which illustrates the initial position of the cutting point as function of r while keeping track of its position upon the drilling progression that includes translation and rotation along z-axis. On the other hand, Figure A.1 (b) illustrates the bottom view of the twist drill bit, where the initial angular position ω can be observed for certain r value.

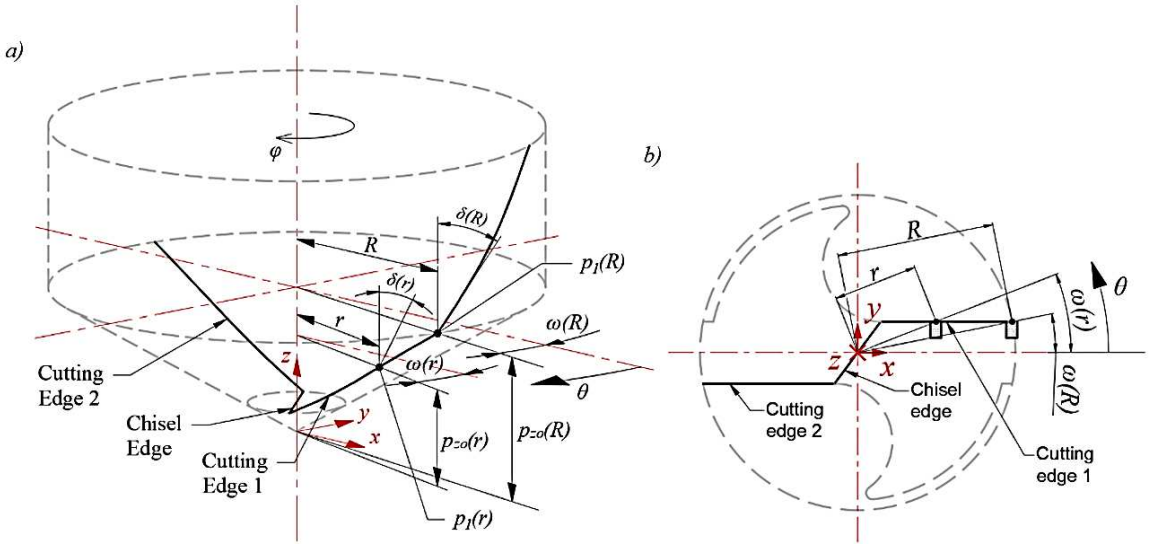


Figure A.1 Cutting point position p_1 on a twist drill. a) coordinate system. b) bottom view of twist drill

Figure A.2 shows the details of geometrical analysis of the machined surface profile that has saw-tooth like profile. Along with this, several equations are shown here to determine several dimensions used to arrive at the equations shown in Section 3.1.

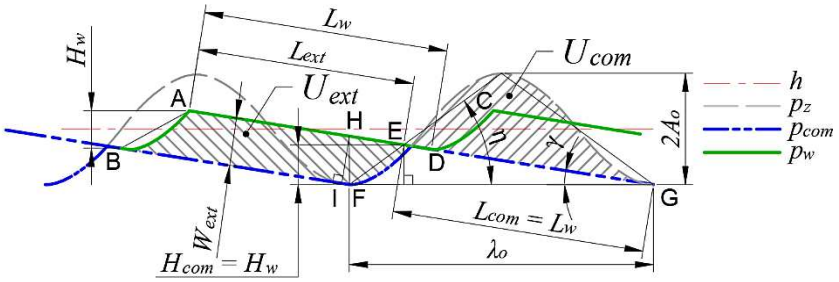


Figure A.2 Illustration of variables to determine the wiped surface function;
(r = 3 mm; γ = 9°; S = 4000 rpm; f_o = 25000 Hz; A_o = 9.3 µm)

The p_{com} shape is first observed from point F to point G. It can be approximated as triangle FEG. Based on the law of sines, it can be shown that

$$\frac{\lambda_o}{sin(\,180° - \gamma - \eta)} = \frac{\overline{EG}}{sin\,\eta}. \tag{24}$$

Noting that

$$\eta = tan^{-1}\left(\frac{4A_o}{\lambda_o}\right) \tag{25}$$

The slope length of p_{com} (L_{com}) which is equal to L_w or EG can be evaluated as:

$$L_w = \overline{EG} = \frac{\lambda_o \sin\eta}{sin(\,180^\circ - \gamma - \eta)}. \tag{26}$$

and the height of profile p_{com} (H_{com}) that is equal to H_w can be evaluated as:

$$H_w = L_w \sin\gamma \tag{27}$$

It is found that the error of H_w under this approximation for the particular case shown in Figure 10 is only 3%, meanwhile, the errors for other applicable cases are within 5%. Thus, it is assumed that the approximation is acceptable to be used.

The compressed volume (U_{com}) can be determined by subtracting the area under the p_z profile from point F to point G with the area of triangle FEG. It can be shown as:

$$U_{com} = A_o\lambda_o - \frac{H_w\lambda_o}{2} \tag{28}$$

Considering the volume conservation, the U_{com} should be equal to the extruded area (U_{ext}). Therefore, parallelogram ABFE represents U_{ext}. Moreover, by observing the triangle *HIF*, the width of the extruded area (W_{ext}) can be shown as:

$$W_{ext} = \lambda_o \sin\gamma \tag{29}$$

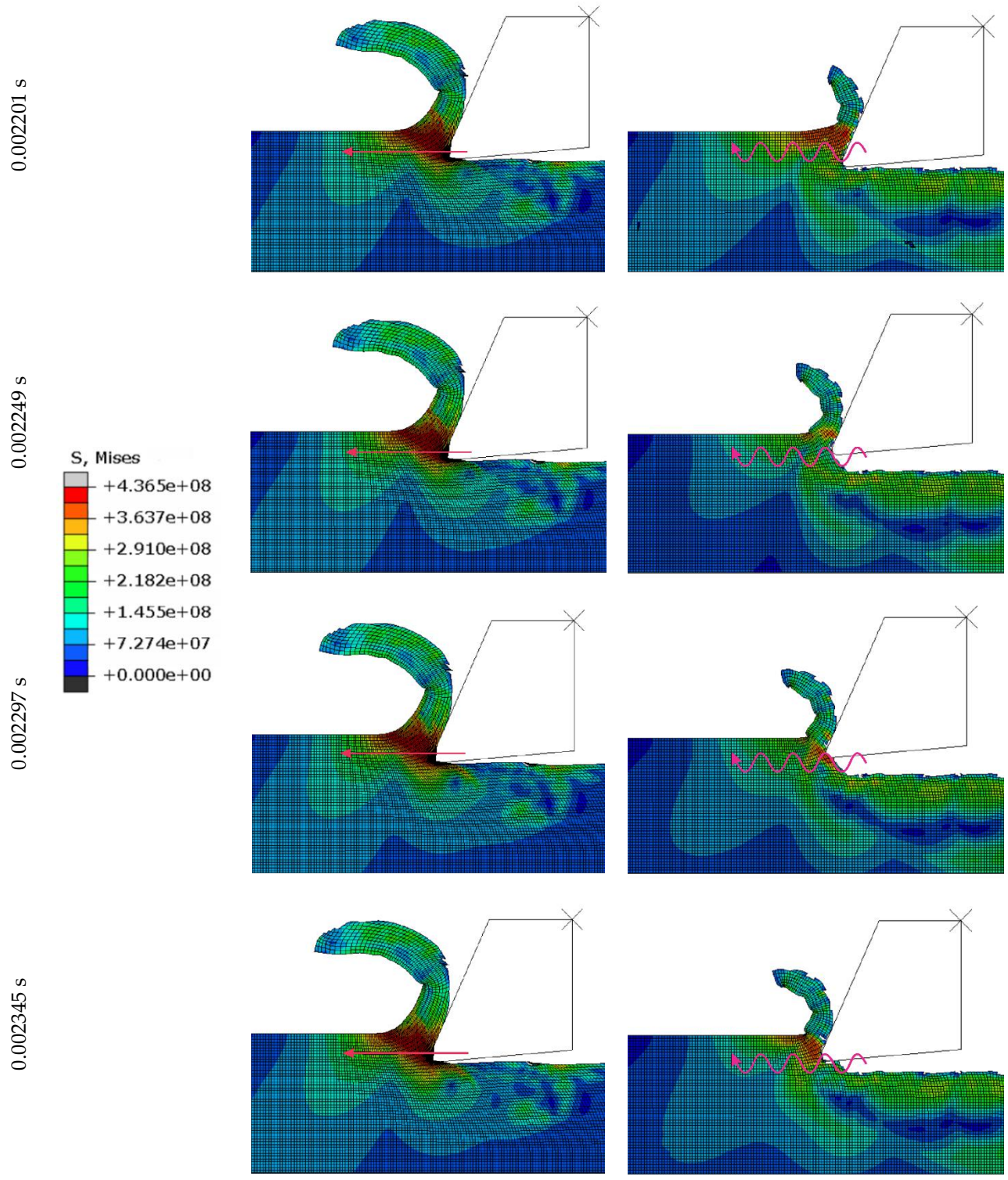
Thus, the length of the extruded area (L_{ext}) can be expressed as:

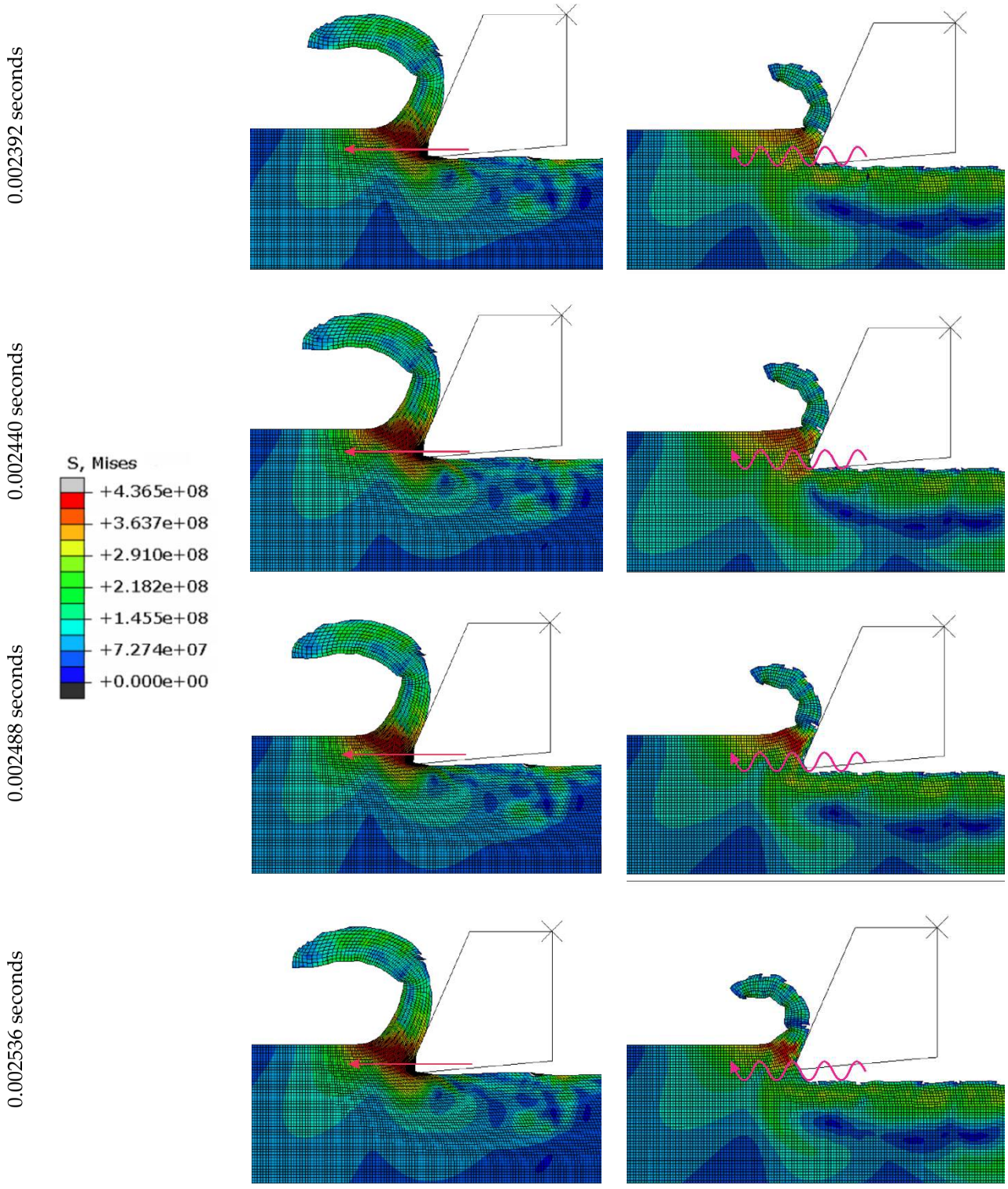
$$L_{ext} = \frac{U_{ext}}{W_{ext}} \tag{30}$$

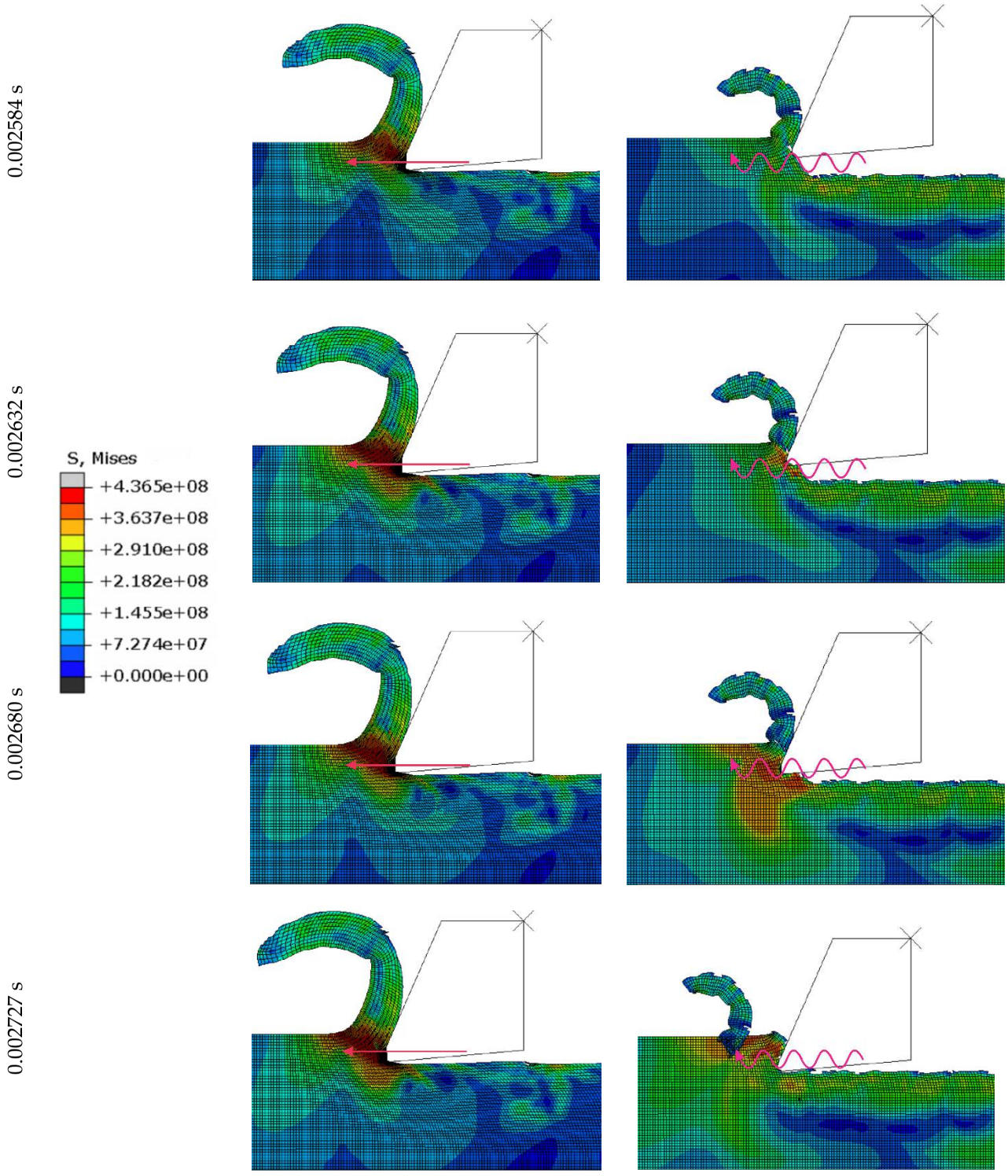
Up to this point, the geometric attributes of the wiped surface profile which are L_w, H_w and λ_o can be evaluated. Moreover, the extruded area and the shape of profile (ABCD) can be determined.

Figure A.3 Finite element analysis at cutting edge during the chip breakage

Figure A3 shows the FEA results for both CD and UVAD within certain simulation time until one chip breakage occurs. The stress plot is shown to be at the same time step for both simulations so that they can be compared. To be compact, the plots only show the stress contour where the chip is already formed until it breaks since this is most important phase. The videos are available as stated in Availability of Data and Materials section.




0.002392 seconds
0.002440 seconds
0.002488 seconds
0.002536 seconds
S, Mises
+4.365e+08
+3.637e+08
+2.910e+08
+2.182e+08
+1.455e+08
+7.274e+07
+0.000e+00


0.002584 s
0.002632 s
0.002680 s
0.002727 s
S, Mises
+4.365e+08
+3.637e+08
+2.910e+08
+2.182e+08
+1.455e+08
+7.274e+07
+0.000e+00